



Parasitic waves and micro-breaking on highly nonlinear gravity–capillary waves in a convergent channel

Chang Xu^{1,2} and Marc Perlin^{1,2,†}

¹Department of Ocean Engineering, Texas A&M University, Galveston, TX 77550, USA

²Department of Ocean Engineering, Texas A&M University, College Station, TX 77843, USA

(Received 7 April 2022; revised 19 March 2023; accepted 5 April 2023)

Gravity–capillary waves are waves influenced by both the effects of surface tension and gravity; these waves are at small scales with wavelength range from approximately 10 cm to less than 1 cm. Gravity–capillary waves play a significant role in air–sea interactions, and they exhibit much different features compared with gravity waves. They can be observed widely on the sea surface. Parasitic waves (capillary waves generated by and that ride on gravity and/or gravity–capillary waves) and micro-breaking can be observed on the water surface with winds; however, the presence of wind makes it difficult to analyse the mechanisms of the wave itself. In this paper, parasitic waves and micro-breaking on gravity–capillary waves are examined experimentally, both in the absence of wind. Parasitic waves and axisymmetric micro-breaking waves are generated mechanically in a convergent channel, where energy density increases due to spatial convergence. Three experimental techniques are used to measure wave properties: planar laser-induced fluorescence, particle image velocimetry and shadowgraphs. The wave profile evolution and vortices beneath the parasitic waves are studied. The micro-breaking of gravity–capillary waves is observed on a surface with added surfactant. The surfactant increases the Bond number, and makes breaking possible in these small-scale waves. Energy dissipation of parasitic waves and micro-breaking is quantified, and the enhanced dissipation caused by parasitic waves is identified through the experiments. In this study, mechanically generated breaking waves with wavelengths less than 10 cm are studied for the first time, without the effect of wind. The results yield insight into wave characteristics and energy dissipation on the air–sea interface at small scales.

Key words: capillary waves, wave breaking, capillary flows

† Email address for correspondence: perlin@tamu.edu

1. Introduction

Steep gravity waves are known to generate capillary waves on their forward faces due to the large curvature across the crests where surface tension becomes locally important. These waves are called parasitic capillary waves. Parasitic capillary waves extract energy from the primary waves through viscous energy dissipation at short scales. There are few research articles on these small waves available in the literature. The early analytical analyses for parasitic waves can be found in Longuet-Higgins (1963) and Crapper (1970). Cox (1958) undertook the first extensive experiments on the generation of capillary waves by longer waves. However, they were mostly approximately wind-generated waves and have different boundary conditions from the free, or mechanically generated waves. Perlin, Lin & Ting (1993) and Jiang *et al.* (1999) performed experimental studies of mechanically generated parasitic waves on gravity–capillary waves, and compared the results with the analytical analysis of Longuet-Higgins (1963) and Crapper (1970). In 1995, Longuet-Higgins (1995) improved his theory and also compared them with the previous experiments. Lin & Perlin (2001) used particle image velocimetry (PIV) to measure the vorticity beneath the parasitic waves, and the results showed agreement with the numerical study by Mui & Dommermuth (1995). These studies all focused on parasitic wave profiles and dealt with parasitic waves in a two-dimensional channel, where the parasitic waves dissipate quickly due to viscosity. Zhang (2002) studied the energy dissipation of the parasitic waves experimentally, but due to the limitations of the experimental methods, only potential energy was considered. Later, Tsai & Hung (2010) studied the enhanced energy dissipation of parasitic waves numerically; they found that the attenuation rate of the carrier wave can increase by more than one order of magnitude in the presence of capillary waves. Thus the generation of parasitic waves significantly increases the dissipation rate of the wave energy. To balance the viscous dissipation and thus achieve steady solutions of parasitic waves, wind forcing is often applied in numerical simulation, as done, for example, by Fedorov & Melville (1998). To verify the model in their paper, experiments on parasitic waves were conducted subsequently by Fedorov, Melville & Rozenberg (1998), which showed good agreement in wave profiles between numerical and physical experiments. Melville & Fedorov (2015) compared the parasitic dissipation and the wind energy in a numerical analysis; the results showed that the dissipation due to the parasitic capillaries is sufficient to balance the wind energy input in some cases. However, adding stationary wind to the water surface is not trivial in experimental studies. More recently, parasitic waves generated by wind were studied experimentally, focusing on the front–back asymmetry of non-breaking gravity–capillary waves (Dosaev, Troitskaya & Shrira 2021). Regardless, experimental study of evolution and energy dissipation of mechanically generated parasitic waves is needed to better understand the mechanics of parasitic waves and their interactions with the primary waves. There is also a lack of experimental evidence of enhanced dissipation of parasitic waves in the literature.

On the other hand, breaking gravity waves in deep water have been studied for decades. One of the most notable contributions in this area is the research by Melville (1982). In his work, Melville experimentally verified that the Benjamin–Feir instability can lead to breaking. However, the fundamental question of determining the onset of wave breaking is still unanswered. For more than two decades, three types of breaking criteria have been used to analyse the breaking (Ramberg, Barber & Griffin 1985; Ramberg & Griffin 1987; Chabane & Choi 2019): geometric, kinematic and dynamic. To produce a breaking wave in the laboratory, often the dispersive nature of gravity waves is used. A wave packet is generated at the wavemaker to produce different frequency components that reach the same location at a given time. This method is widely used in laboratories to

generate steep and breaking waves. One famous example is by Rapp & Melville (1990), which provided remarkable insight into wave breaking. For three-dimensional breaking, She, Greated & Easson (1994) and Wu & Nepf (2002) used spatial focusing to generate breaking gravity waves; they found that spatial focusing increased the steepness onset of wave breaking. Nepf, Wu & Chan (1998) used a phase-shifted wavemaker array to generate three-dimensional waves and their subsequent diffraction to generate breakers. Due to an increase in particle velocity, the steepness onset of breaking is decreased.

Unlike geometric or kinematic onset, the dynamic onset is more consistent; the difficulty is that the kinetic energy cannot be measured easily in experiments. Iafrati (2009) developed a numerical model to calculate the energy dissipation during the breaking process. He found that in the most energetic phase of plunging breaking, dissipation is mainly localized approximately in the small air bubbles generated by the fragmentation of the air cavity entrapped by the plunging of the jet. The air-entry phenomenon was later reviewed by Kiger & Duncan (2012). Derakhti & Kirby (2014) studied air entrainment using a two-phase model. Later, Derakhti & Kirby (2016) presented direct estimates of total energy and momentum flux in unforced deep-water unsteady breaking waves generated by dispersive focusing. More recent work on breaking onset can be seen in Barthelemy *et al.* (2018) and Derakhti, Banner & Kirby (2018). Although the experimental study of breaking onset is difficult, there are a few contributions in the literature: Duncan (2001) used PIV to measure the flow field in a spilling breaker; he found that particle velocity is slower than the phase velocity at incipient breaking. Lim *et al.* (2015) used PIV to measure the velocities and void fraction under an unsteady deep-water plunging breaker. Khait & Shemer (2018) and Saket *et al.* (2017) used experiments to verify the kinematic criterion presented by Barthelemy *et al.* (2018). Na, Kuang-An & Ho-Joon (2020) studied the kinematics and breaking onset of spilling breakers using PIV; this study found that the ratio of potential energy to the total energy remained close to 0.5 throughout the breaking process.

Surface tension plays a significant role in wave breaking, especially for shorter waves. Experimental study of surface tension effects on breaking waves can be found in an early work by Miller (1973). In shorter waves, spilling breakers can be observed more frequently than plunger breakers, and they are a more important contributor to turbulence, spray and bubble generation at the water surface. Duncan *et al.* (1999) studied the crest profile of spilling breakers. Liu & Duncan (2003) studied spilling breaking waves under varying surface tension. They found that a high surfactant concentration on the surface will change a spilling breaker to a plunger breaker. More recently, Deike, Popinet & Melville (2015) developed a direct numerical simulation method for wave breaking simulation. By introducing surface tension into the model, capillary effects on wave breaking were studied. Bond number and steepness were used to distinguish the three types of waves: spilling, plunging and waves with parasitic capillary waves. The high dissipation rate of parasitic waves was observed using numerical simulation, but the study did not involve micro-breaking. Rather, it showed that most of the cases under low Bond number show parasitic capillary waves. There is a lack of experimental data for low-Bond-number (gravity–capillary) breaking waves. Other than plunging and spilling breakers in gravity waves, micro-breaking happens on short waves and is less intense (Babanin 2011). Most of the previous numerical and experimental studies of breaking waves focused on gravity waves. There are very few studies of breaking or micro-breaking waves for wavelengths less than 20 cm, either due to the difficulties in the experiments or due to the subtlety of the breaking process itself. Zappa, Asher & Jessup (2001) studied the energy dissipation and spectral properties of wind-generated micro-breaking waves; infrared images were used

to identify micro-breaking (see Siddiqui *et al.* 2001; Jessup *et al.* 1997). Laxague *et al.* (2018) studied the spectral characteristics of gravity–capillary waves with wind-generated micro-breaking through field observations. The presence of wind makes the analysis of micro-breaking much more complicated. Also, breaking waves at gravity–capillary scales without wind are basically unexploited in the literature. Experimental studies are needed to answer the following questions: Will gravity–capillary waves break in the absence of wind? If they do not break, why? If they do break, how is the breaking different from the breaking in gravity waves?

In this work, the parasitic waves and micro-breaking of gravity–capillary waves are studied experimentally. Using spatial convergence, steep and breaking axisymmetric gravity–capillary waves are generated mechanically (in the absence of wind). The geometric features, vorticity and energy dissipation caused by the parasitic waves are analysed. On a surface with added surfactant, breaking occurs on waves with wavelengths less than 10 cm. The energy dissipation and geometric and kinematic features during the micro-breaking process are studied. Geometry of the wave profiles and the phase speed are measured by planar laser-induced fluorescence (PLIF), while the flow fields and vorticity beneath the interface are measured and quantified by PIV. This paper is organized as follows. Section 2 discusses the experimental set-up. Section 3 presents the experiments of parasitic waves on a water surface without added surfactant. In § 4, micro-breaking of gravity–capillary waves is presented, with some comparison between parasitic waves and micro-breaking. Conclusions are drawn in § 5.

2. Experimental set-up

The experiments are conducted in a convergent wave tank, as shown in figure 1. A circular sector wavemaker is used to generate axisymmetric spatially convergent waves; the radius of the curve is 30 cm and the sector angle is 60° . To avoid a singularity, at the end of the tank, there is an extension channel, which has a width of 1.5 cm and length of 8 cm. The tank height is 6.5 cm and the water depth as used is 5 cm. For the frequencies used here, 4–8 Hz, all waves can be considered deep-water waves. The sidewalls of the tank are coated with a hydrophilic material; this helps the sides satisfy (almost) a full slip condition and minimize the dissipation caused by friction and by the contact lines. The circular sector wavemaker is three-dimensionally printed and is attached to an electrodynamic shaker (Modal Shop, Model 2110E) that provides vertical (here sinusoidal) excitation from 4 to 8 Hz. A high-speed imager (Phantom VEO340L) operating at 1500 frames per second with a 50 mm $f/1.8D$ lens (Nikon AF Nikkor) is used to record the required images for all three techniques mentioned below. The high-speed imager is placed above or on the side when viewing through the side of the transparent tank, depending on the technique used. The wavemaker has an immersion depth of 10 mm; its cross-section is shown in figure 2(b). The coordinate system used herein is shown in figure 2: the origin is defined at the starting point of the fixed laser sheet; the longitudinal direction of the wave tank is the x axis; the lateral direction is the y axis; the z axis points vertically upward from the free surface. The control signals are generated by a National Instruments cRIO-9067 system and LabView software. The experimental set-ups are shown in figure 2. Three non-invasive wave measurement techniques are used in these experiments, listed as follows.

(i) PLIF

A continuous laser sheet is projected from above the tank; the laser sheet is aligned with the centre of the tank, as shown in figure 2(a). The high-speed imager records

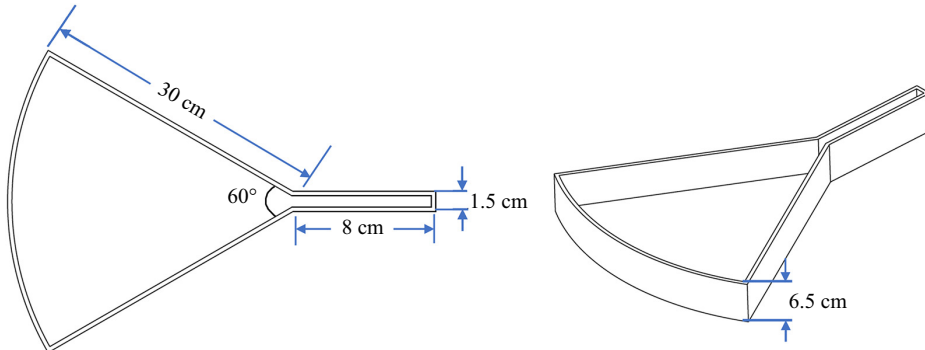


Figure 1. Convergent wave tank: plan and oblique views.

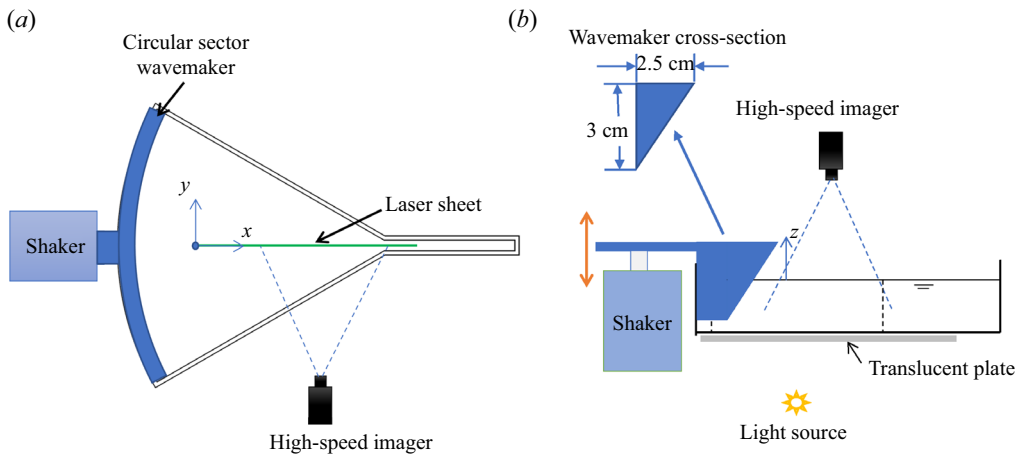


Figure 2. Experimental set-up for (a) PLIF and PIV (plan view) and (b) shadowgraph (side view) techniques. The x axis is along the propagation direction, the y axis is along the lateral direction and the z axis is pointing upwards. Note that the paddle is curved and its projection is as shown in (b).

frames through the side of the tank. The laser-sheet-illuminated area and the view area of the camera can be adjusted. In this study, the laser sheet is fixed for all experimental cases to unify the coordinates. This technique is able to accurately capture the wave profiles along the laser sheet. This provides information required for the wave profile and potential energy calculations.

(ii) PIV

Tracking particles (glass hollow spheres) of diameter from 9 to 13 μm are added to the water. Using the same laser sheet and imager set-up introduced for PLIF, the velocity field and thus the vorticity field within the waves can be determined from the acquired images using DaVis software from LaVision. This also provides information required for wave kinetic energy evaluation.

(iii) Shadowgraphs

A translucent plate is positioned beneath the tank, between the light source and the water, as shown in figure 2(b). The imager captures the frame from above. This technique exhibits the three-dimensional wave pattern present on the surface.

It provides a qualitative measurement of the two-dimensional free surface; this is required when the surface becomes non-axisymmetric due to instability or breaking.

To analyse the surface tension effect on the parasitic waves and wave breaking, surfactant is added in some experiments as noted. In this study, Triton X-100 is used as the surfactant. The surface tensions of treated and untreated water surfaces are inferred via linear wave theory, by measuring the wavelength of a mechanically generated linear wave, and using the linear dispersion relation with the frequency used at the wavemaker.

3. Parasitic waves formed by highly nonlinear gravity–capillary waves

Capillary waves riding on longer gravity carrier waves are commonly observed on ocean surfaces. These parasitic capillary waves, with length scales ranging from a few centimetres to fractions of millimetres, can be distributed over the entire surface or located on the leading slope of the carrier waves. The parasitic waves are caused by surface tension: the surface tension acts as a pressure source on the water surface. To first order, the pressure is proportional to the curvature of the surface, and as the pressure moves with the crests, it generates capillary waves on the forward side of the crest. These forced parasitic waves move at approximately the same phase speed as the primary carrier waves. Thus, in a reference frame moving with the crest, the parasitic waves are almost steady, except they dissipate as the wave propagates. Parasitic capillary waves have been studied for decades; however, most previous work focuses on two-dimensional, wind-generated waves. When wind is absent, parasitic waves generated by steep waves dissipate quickly due to viscosity. In the configuration used herein, the axisymmetric primary waves are generated mechanically in a convergent channel, where the energy density of the primary waves increases as they propagate, and thus generate the parasitic waves. This compensates for part of the dissipation and causes the parasitic waves to steepen downstream. At the same time, high vorticity can be observed under the parasitic waves and the energy of the primary wave is dissipated through these parasitic waves.

3.1. Profile evolution of parasitic waves

The wave profile evolution in the convergent tank is obtained using the PLIF technique. The method is similar to that used in Perlin *et al.* (1993), Xu & Perlin (2021), Duncan *et al.* (1999) and many others. The accuracy of the measurement primarily depends on the optical distortion and the image resolution. To evaluate the induced distortion caused by the optical devices in this study (one lens and two doublets and the imager itself), the calibration targets captured in the same plane as the laser sheet are shown in [figure 3](#). [Figure 3](#) shows two recorded images of the precision 4 cycles mm^{-1} lines used to calculate resolution, and as is evident neither horizontal nor vertical images show noticeable distortion. The resolution of the images is 14.2 pixels mm^{-1} ; hence, the accuracy of the wavelength measurement is ± 0.07 mm. The precision of the surface measurement technique is also impacted by the width of the laser sheet (measured to be 0.5 mm in the present study), as the camera is not perfectly aligned parallel to the water surface. To assess the measurement error, a plano-convex lens with known geometrical shape (Newport KPX184) is utilized. The lens is coated with white paint to facilitate illumination of the surface with the laser sheet, replicating the illumination of a dyed water surface. The laser sheet is projected to the centre line of the lens. [Figure 4\(a\)](#) shows one frame of the image captured by the high-speed imager. The surface profile is extracted using the edge detection method, which identifies the points where the gradient of the image is maximum.

Parasitic waves and micro-breaking on gravity–capillary waves

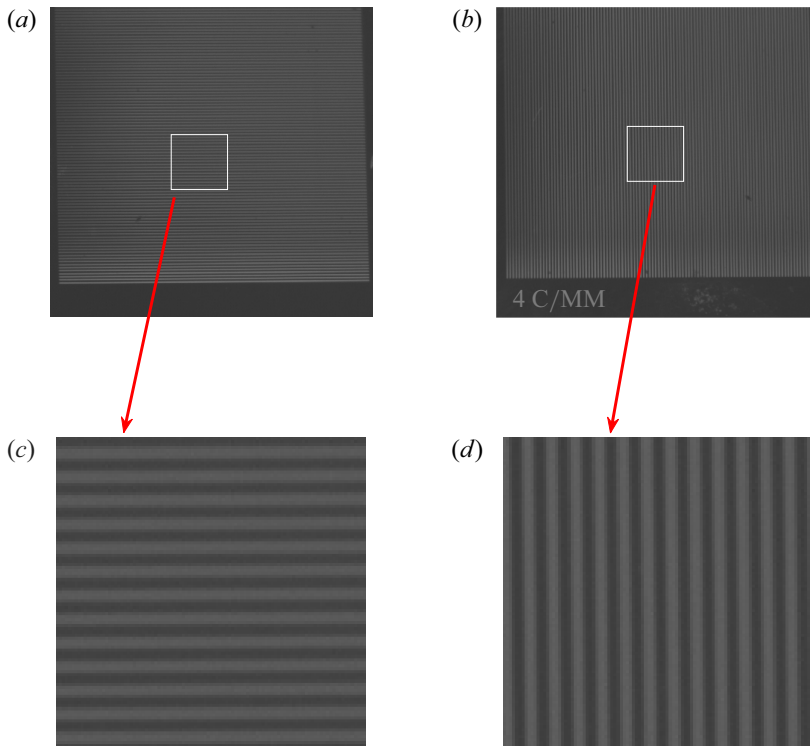


Figure 3. Recorded images of precision Ronchi rulings (4 cycles mm^{-1}) used for calibrations. (a,c) Horizontal lines. (b,d) Vertical lines.

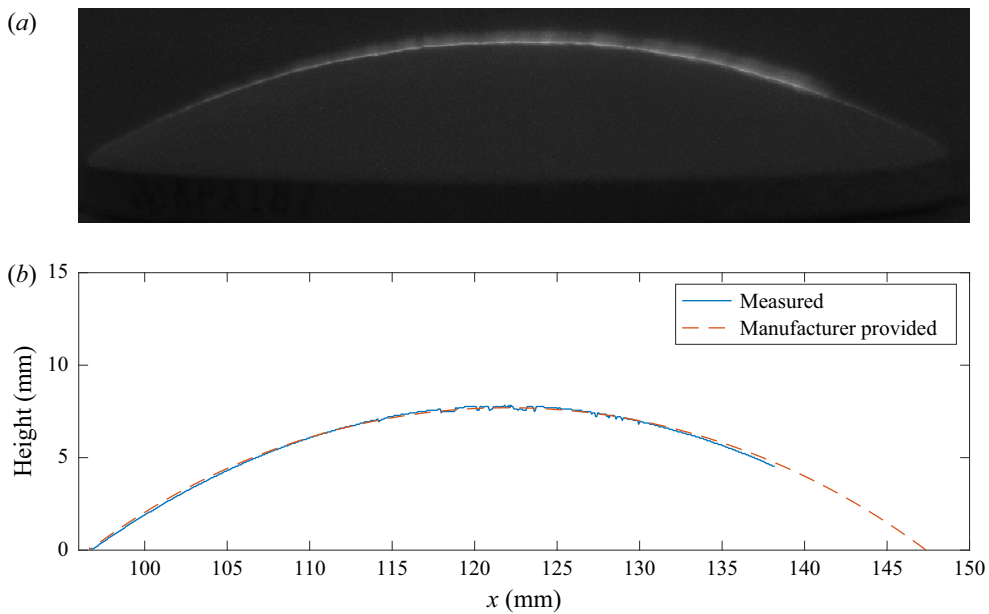


Figure 4. Surface profile of a plano-convex lens measured by PLIF compared with manufacturer-provided profile. (a) Recorded image. (b) Surface profiles.

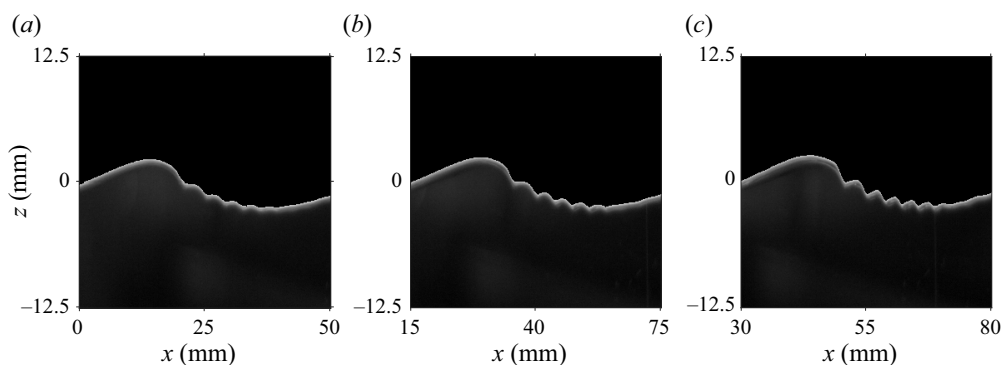


Figure 5. Parasitic wave evolution on a 5.5 Hz wave. The vertical dimension of the picture is exaggerated by a factor of two.

The image clearly depicts a bright line that indicates the illuminated surface. However, due to the finite width of the laser sheet and the oblique angle of the imager, the bright line appears to be of finite thickness. Therefore, to obtain an accurate surface profile, the lower boundary of the bright line is considered while applying the edge detection method. The extracted surface profile is plotted with the exact profile provided by the manufacturer, as shown in figure 4(b). The measured result shows excellent agreement with the true value. The root mean square of the error (defined as $R = \sqrt{1/N \sum_{i=1}^N (\eta_{mi} - \eta_{pi})^2}$, where η_{mi} are the measured surface points and η_{pi} are the manufacturer-provided surface points) is calculated to be 0.05 mm. In the figure, it is seen that the measurement does not cover the entire length of the lens surface, which is due to the limited length of the laser sheet. In the context of water surface measurements, the lower edge of the illuminated line corresponds to the air–water interface, and the thickness of the line is a result of the laser sheet’s reflection above the surface. As such, accounting for the lower boundary of the bright line yields a more precise surface profile measurement. In practical applications, different thresholds are utilized to optimize the performance of the edge detection algorithm for each particular case. It is also important to acknowledge that the angle of the free surface can impact the accuracy of the measurement. In extreme cases where the free-surface angle reaches or exceeds 90° , it is possible that part of the surface may not be illuminated, thus impacting the measurement. However, in this study, the parasitic waves did not have a significant impact on the measurement accuracy as they were not steep enough to block illumination. Therefore, the steepness of the parasitic waves is not a significant factor in affecting the measurement accuracy.

The PLIF results for 5.5, 6, 6.5 and 7.5 Hz waves are shown in figures 5 and 8. To better visualize the parasitic waves, the vertical dimensions of these pictures are exaggerated by a factor of two. The x axis is defined along the laser sheet, starting from the upstream intersection of the laser sheet with the free surface, which is 147 mm to the circular centre of the sector. From figure 5, it can be seen that in the early stage, the wave crest is smoother, small parasitic ripples can be observed (figure 5a) and the crest is 15 mm downstream (i.e. $x = 15$ mm). As the crest moves further and the wave converges more, the parasitic waves along the forward face of the crest continue to grow.

A quantitative comparison of the wave profile at different positions is shown in figure 6. It can be seen that the parasitic waves become significantly steeper as the wave propagates. To obtain a better view of the parasitic waves themselves, a plot of parasitic waves only is shown in the figure inset. The pure parasitic waves are obtained by empirical

Parasitic waves and micro-breaking on gravity–capillary waves

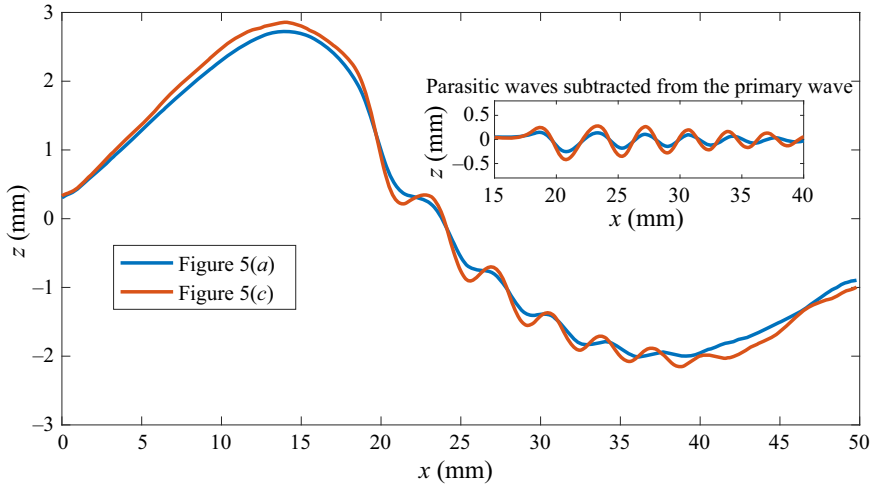


Figure 6. Parasitic waves on a 5.5 Hz wave. Waves in the inset are obtained by subtracting the primary underlying wave from the wave profile.

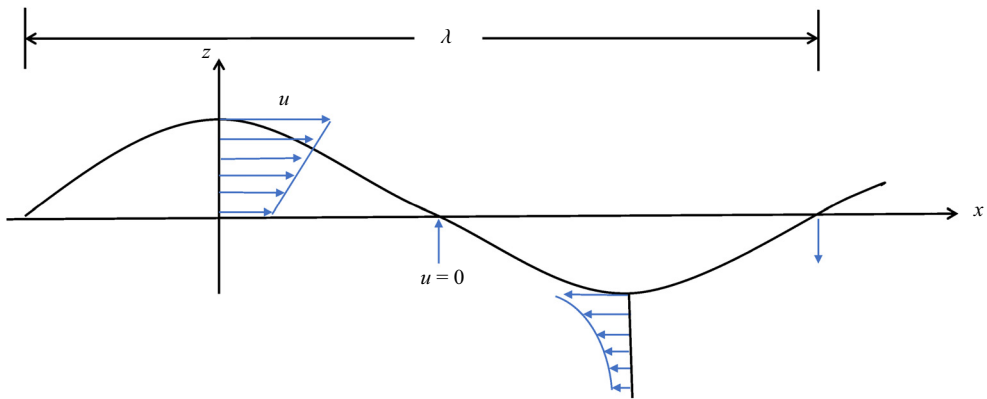


Figure 7. Horizontal particle velocities beneath the crest and trough in a progressive wave propagating to the right. Only the uppermost velocities are depicted.

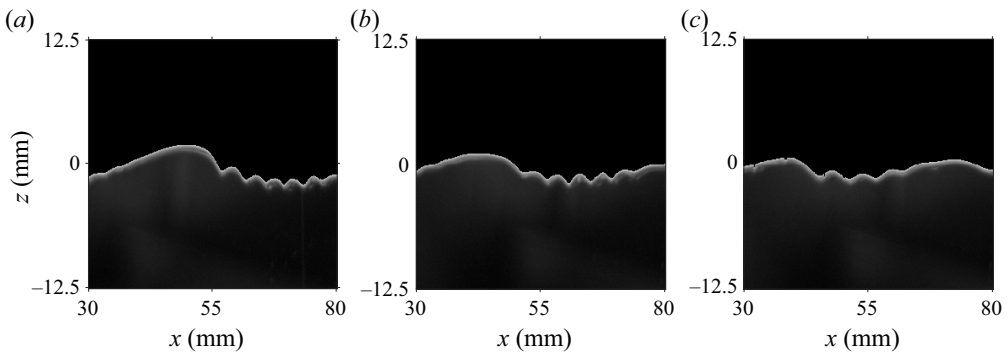


Figure 8. Parasitic ripples on (a) 6 Hz, (b) 6.5 Hz and (c) 7.5 Hz waves. The vertical dimension of the image is exaggerated by a factor of two.

mode decomposition (EMD). The EMD technique is a signal decomposition method first introduced by Huang *et al.* (1998); it has been used widely in multicomponent signal analysis. Unlike traditional frequency-based filters, it identifies wave components by a so-called sifting process, which extracts intrinsic mode functions from the local maximums and minimums of the original signal. One of the key advantages of this method is that it can extract components with varying frequencies, in this case, wavenumbers. As the wavenumber of the parasitic waves change in space, EMD becomes a suitable method to obtain pure parasitic waves from the original wave form. In this study, only one sifting iteration is used and the parasitic component of the wave is the first intrinsic mode function. It can be seen in [figure 6](#) that the parasitic wave crest phases do not change as they steepen. The maximum steepness of the parasitic waves can be obtained from the figure. They are $ka = 0.21$ for the blue profile and $ka = 0.43$ for the red profile. The parasitic waves have different wavelengths along the same primary wave; the wavelengths are longer near the top of the crest and shorter towards the trough. This is due to the variation in the underlying current beneath the carrier wave. The particle velocities generated by the primary wave act as underlying currents for the parasitic capillary waves. Near the crest, under the first parasitic wave crest, the underlying current has a maximum velocity to the right; in the region where the surface goes through $z = 0$, the horizontal component of the particle velocity is zero; beneath the trough, the underlying current is maximum to the left, as shown in [figure 7](#) (Dean & Dalrymple 1991). It is well known that waves get stretched when they propagate in the same direction as an underlying current, and are shortened when they propagate opposite it. The parasitic waves steepen as the carrier wave propagates towards the tank extension, rather than dissipate and disappear as in two-dimensional cases. As can be seen from [figures 5 and 6](#), the amplitude of the primary wave remains almost unchanged, which is counter-intuitive as the channel converges. It is reasonable to conclude that the energy density gained by spatial convergence is mainly dissipated by the parasitic waves. They have much greater wavenumber, and according to viscous linear wave theory, the dissipation rate is proportional to the square of the wavenumber. Thus, the parasitic waves dissipate at a much greater rate due to viscosity compared with the primary waves. This is quantitatively studied in the following section. It is also worth noting that the steepness of the parasitic waves does not increase continuously; rather, it decreases once the steepness reaches a maximum. The maximum steepness for each case is discussed in the next section.

Parasitic waves on primary waves of different frequencies are shown in [figure 8](#). It can be seen that the wavelengths of the parasitic waves increase with the primary wave frequency. This is consistent with the theory that the parasitic waves satisfy the dispersion relation and travel at the same phase speed as the primary waves. Theoretically, if surface tension is considered, there will be a minimum phase speed for water waves (around 0.23 m s^{-1}). For each phase speed greater than the minimum speed, there are two corresponding wavenumbers; details are shown in [figure 10](#). Similar to [figure 6](#), the wave profiles are shown quantitatively in [figure 9](#). The parasitic wave profiles are obtained by EMD. For a better comparison, in the parasitic wave inset plot, the waves are aligned so that the first crests start at the same location. The amplitude of the primary wave decreases significantly with the excitation frequency. However, the amplitudes of the parasitic waves are similar for different frequencies. It can also be seen that, although the wavelength of the primary wave decreases with the excitation frequency, the wavelength of the parasitic waves increases with the frequency. As can be inferred from [figure 10](#), each gravity–capillary wave has a corresponding resonant capillary wave that travels at the same phase velocity (i.e. each phase speed other than the minimum has two associated wavenumbers).

Parasitic waves and micro-breaking on gravity–capillary waves

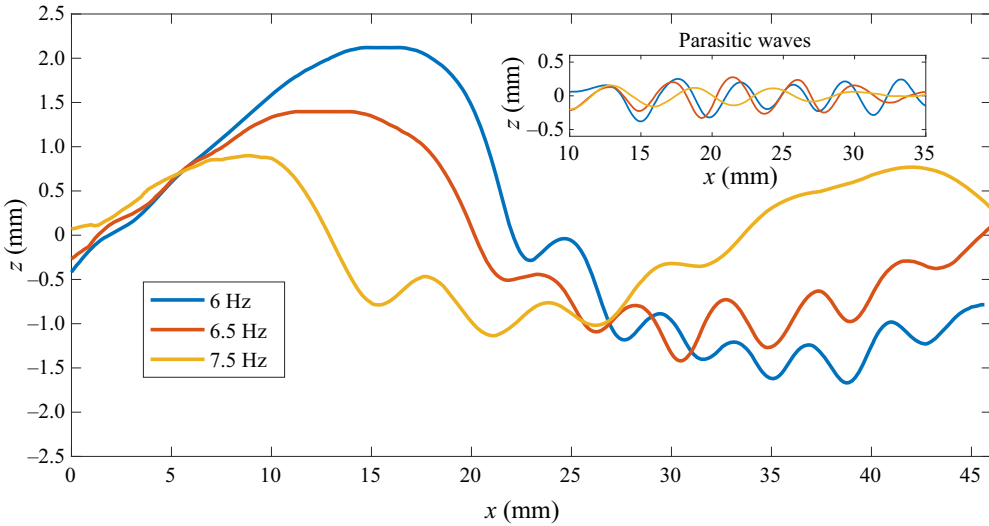


Figure 9. Parasitic ripples on 6, 6.5 and 7.5 Hz waves. The initial point of each wave is aligned so that they all start approximately near the mean water level.

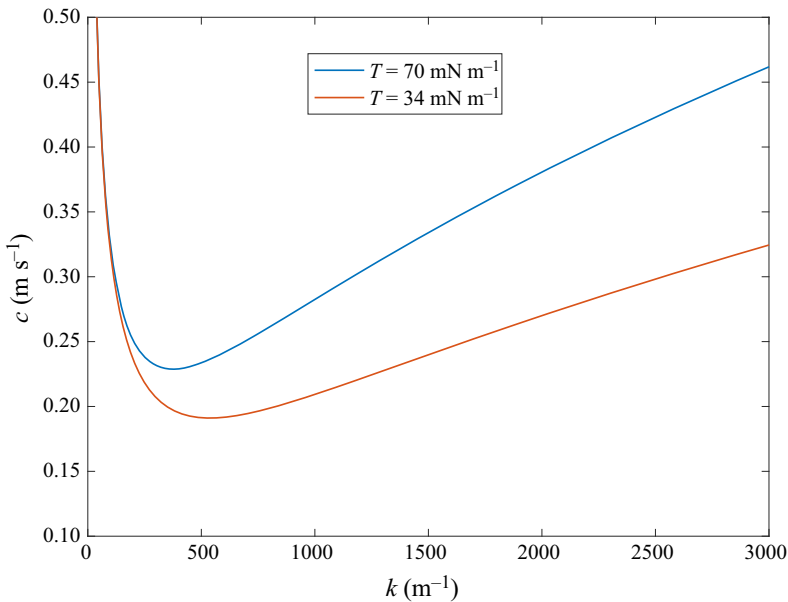


Figure 10. Dispersion relation with and without surfactant. Blue curve: filtered water without added surfactant; red curve: filtered water with added surfactant.

The red curve shows the dispersion relation for a surface with surfactant and is discussed subsequently.

The steepness, wavelength and Bond number of each experimental case without surfactant are summarized in [table 1](#). To obtain the steepest primary wave and the parasitic waves in each experimental condition, for all cases, the wavemaker stroke is established so that it generates the steepest axisymmetric wave without parasitic waves at the very first crest near the wavemaker. Here, the Bond number is defined as $Bo = \rho g / Tk^2$, where

Case number	Frequency (Hz)	$ka_{primary}$	$ka_{parasitic}$	$\lambda_{primary}$ (cm)	$\lambda_{parasitic}$ (cm)	Wavelength ratio	Bo
1	4.5	0.25	0.48	7.91	0.33	24.0	22.9
2	5.5	0.29	0.56	5.62	0.43	12.2	11.2
3	6.0	0.26	0.65	4.85	0.44	11.0	8.34
4	6.5	0.22	0.66	4.26	0.46	9.26	6.45
5	7.0	0.23	0.66	3.77	0.54	6.98	5.13
6	7.5	0.24	0.69	3.44	0.59	5.83	4.19

Table 1. Parameters of primary and parasitic waves in the convergent channel (on a water surface without surfactant).

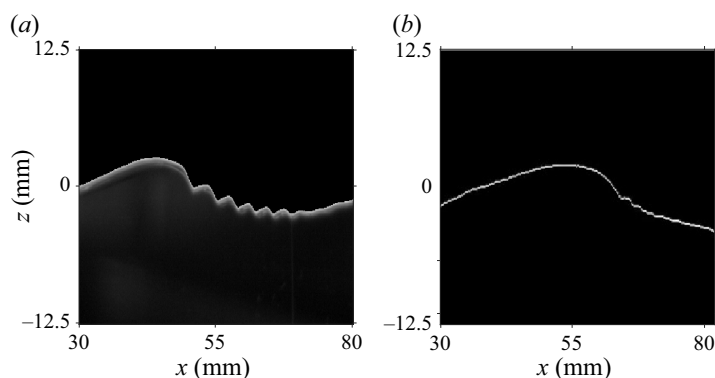


Figure 11. Parasitic ripples on a 6 Hz wave (a) without and (b) with surfactant. The vertical dimension of the picture is exaggerated by a factor of two.

ρ is the mass density of water, g is the acceleration of gravity, T is the surface tension and k is the wavenumber. The steepness of the primary waves, $ka_{parasitic}$, is calculated at the instant when the steepness of the first parasitic wave reaches its maximum. The wavelengths of the parasitic waves, $\lambda_{parasitic}$, are measured at the mean water level. As the frequency of the primary wave generated increases, the wavelength of the primary wave is closer to the wavelength of the parasitic waves. As shown in table 1, the wavelength ratio of the carrier wave to the first parasitic wave decreases as the frequency of the primary wave increases. At a certain level, the two waves interact with each other and lead to much more complicated surfaces. As Longuet-Higgins (1995) wrote: ‘At basic wavelengths less than approximately 12 cm there may be appreciable interference between the capillary waves generated at adjacent crests of the basic wave.’ For primary waves greater than approximately 8 Hz, it is not easy to differentiate the primary wave crests from the parasitic wave crests. These waves are not presented. It is also shown in table 1 that, for similar primary wave steepness, the maximum steepness of the parasitic wave increases with the frequency; in other words, shorter primary waves generate steeper parasitic waves. The wavelengths of the parasitic waves are of the order of 0.5 cm; thus, they are essentially pure capillary waves.

As wave breaking was not evident in the convergent waves, another approach was warranted. Adding surfactant will significantly decrease the surface tension and thus cause the gravity–capillary wave profiles to more closely resemble those of gravity waves; the surfactant suppresses the formation of parasitic ripples by reducing the pressure caused

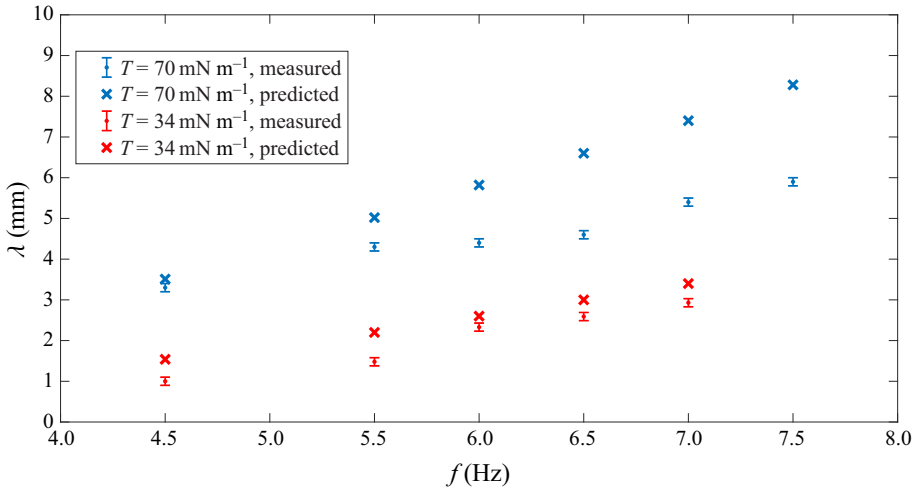


Figure 12. Wavelengths, λ , of parasitic ripples: predicted and measured. Blue cross: predicted wavelength on clean water; red cross: predicted wavelength on water with added surfactant; blue square: measured wavelength on clean water; red square: measured wavelength on water with added surfactant. Error bars are shown for the measured data.

by surface tension. Figure 11 shows two 6 Hz waves captured at the same location, one with clean filtered water (figure 11a) and one with surfactant (figure 11b). As can be seen from the figure, the crest of the wave with surfactant leans further forward, and the first bulge is further downstream compared with the no-surfactant case. The surface tension with surfactant is measured to be 34 mN m^{-1} . In this case, a new dispersion relation is obtained (red curve in figure 10). The parasitic waves in the presence of surfactant are much shorter than those in the clean water case, and the shorter parasitic waves satisfy the new dispersion relation. This is verified by experiments shown below. According to Longuet-Higgins (1995), the parasitic waves are free waves on top of the current generated by the primary wave, and travel at the same speed as the primary waves in the horizontal direction. The condition of resonance can be obtained by approximately matching phase speeds between the longer wave and the shorter capillary wave (Fedorov & Melville 1998). The wavelengths of the parasitic waves vary from the crest to the trough: longer on the crest and shorter on the trough due to the effect of the underlying current. The wavelength of the parasitic waves at the mean water level (where the underlying current is approximately zero in the horizontal direction) is measured, and is compared with those predicted by the dispersion relation. The results are shown in figure 12. Error bars are shown for the measurement results in figure 12. Blue crosses represent the data from the filtered clean water surface ($T = 70 \text{ mN m}^{-1}$) and red squares represent data from the water surface with added surfactant ($T = 34 \text{ mN m}^{-1}$). It can be seen in the figure that the measured wavelengths agree reasonably well with the predicted ones. The wavelengths of the parasitic waves increase with the primary wave frequency. Figure 12 also shows that the wavelengths measured in the added surfactant cases agree better with the predicted ones than those measured in clean water cases, especially for frequencies above 6 Hz. This is because in the clean water cases, according to the dispersion relation (figure 10, blue curve), the phase speed near these frequencies is close to the minimum phase speed. This causes the variation of phase speed to be critical in obtaining the wavelength of the parasitic waves, and hence the prediction becomes less accurate. In the cases with

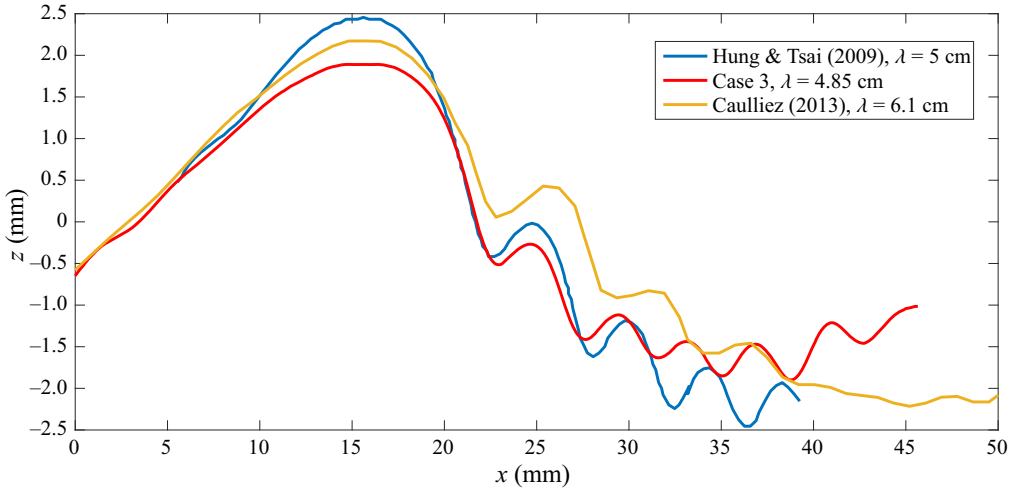


Figure 13. Comparison of the wave profiles of the numerical result obtained by Hung & Tsai (2009, figure 9d), the experimental results in Caulliez (2013, figure 4b) and in the present study. The blue curve shows numerical results for $\lambda = 5$ cm, $ka = 0.28$; the red curve shows the experimental results for $\lambda = 4.85$ cm, $ka = 0.26$; and the yellow curve shows experimental results for $\lambda = 6.1$ cm, $ka = 0.22$.

added surfactant, these frequencies are further from the minimum phase speed and so the prediction is more accurate. Nonlinearity leads to the local resonant condition differing for different phases of the longer-wave profile. Unlike lower frequencies, the parasitic waves on a 7 Hz primary wave have a wavelength of the same order as that of the primary wave itself. This causes significant interactions between parasitic waves and the primary waves. At higher frequencies, the interaction becomes stronger and the wave surface becomes irregular; it is difficult then to differentiate the primary waves and the parasitic waves.

Although there are very few experimental results for mechanically generated parasitic waves in the literature, wind-generated ones and numerical results are available. Figure 13 shows a comparison of the wave profile of the numerical result obtained by Hung & Tsai (2009), the experimental results in Caulliez (2013) and case 3 in the present study. Although the wavelength and steepness of the three studies are not identical, the comparison is still worthwhile as they show similar parasitic wave patterns. Similar to the experimental ones, in the numerical results, the steepest parasitic wave occurs adjacent to the primary crest. It should be noted that the present study is conducted in a convergent channel while most of the studies in the literature are either two-dimensional or in a rectangular tank.

To compare the wave profiles in detail with the previous findings in the literature, another definition of parasitic wave steepness, θ_r , is used. Slope θ_{max} is the maximum slope of the first parasitic wave profile, θ_{min} is the minimum slope and $\theta_r = 0.5(\theta_{max} - \theta_{min})$. A schematic illustration of the definition of θ_r is shown in figure 14. Table 2 summarizes the parasitic wave parameters for several studies. The parameter used in different studies is not the same; here only the results with the closest wavelength and original steepness to the present study are compared. The data values cited for Zhang (1995) and Caulliez (2013) are measured from the wave profiles reported in the literature. It can be seen in the table that mechanically generated parasitic waves in a rectangular channel have the smallest θ_r , while higher wind speed generates greater θ_r . The parasitic waves generated in a convergent channel have a similar θ_r compared with those generated by wind. This is due

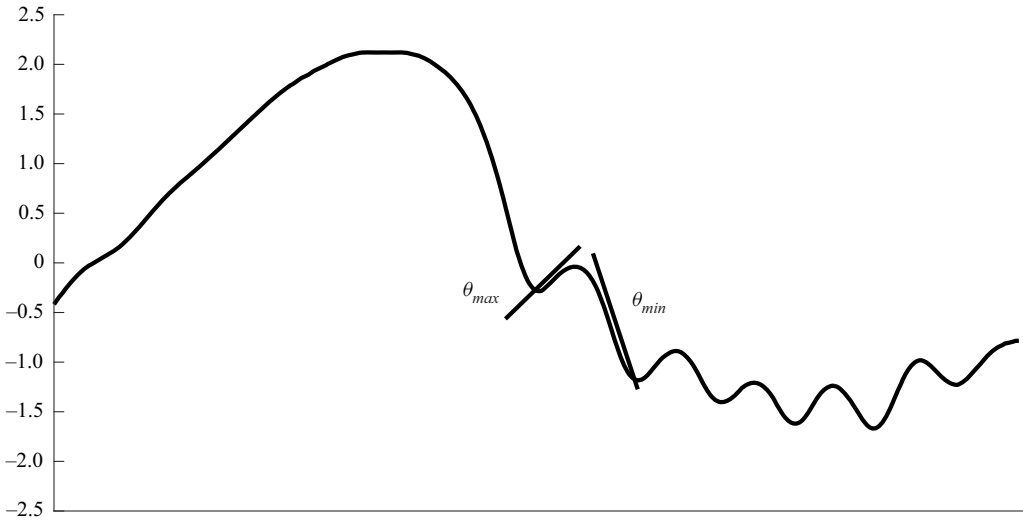


Figure 14. A schematic illustrating the definitions of θ_r . The steepness of the capillary ripple on the forward face of the primary wave immediately adjacent to the crest, θ_r , is defined as $\theta_r = 0.5(\theta_{max} - \theta_{min})$, where θ_{max} and θ_{min} are the maximum and minimum slopes along the ripple surface, respectively.

	$\lambda_{primary}$ (cm)	$ka_{primary}$	θ_r	Generation method
Zhang (1995)	5	0.25	0.45	Wind (9.7 m s ⁻¹)
Fedorov & Melville (1998)	5	0.2	0.10	Mechanical, rectangular
Jiang <i>et al.</i> (1999)	4.72	0.15	0.27	Mechanical, rectangular
Hung & Tsai (2009)	5	0.24	0.33	Numerical
Cauliez (2013)	6.1	0.22	0.30	Wind (5.0 m s ⁻¹)
Present	4.85	0.26	0.47	Mechanical, convergent

Table 2. Parameters of primary and parasitic waves in different studies. The data values cited for Zhang (1995) and Cauliez (2013) are measured from the wave profiles reported in the literature.

to that in the wind-generated cases, energy dissipated by parasitic waves is offset by wind, while in the convergent channel, the energy density is increased by spatial convergence.

3.2. Vorticity beneath parasitic waves

When parasitic waves form, they perturb the particle velocities, and develop vorticity beneath the primary waves. The vorticity contributes to primary wave instability and energy dissipation. In this section, the identification of primary and parasitic wave profiles was accomplished utilizing the same edge detection algorithm detailed in the previous section. It is worth noting that the use of dye was not necessary in this section. Rather, seeding particles were employed in PIV, which have a slightly lower density than water, resulting in a higher concentration of particles on the free surface relative to the bulk water. This concentration gradient results in a clear illuminated boundary when the laser sheet is in operation, as depicted in figures 15–17. The thickness of the illuminated boundary is influenced by the thickness of the laser sheet and the reflections on the surface. The efficacy of the edge detection technique in obtaining highly accurate surface profiles has

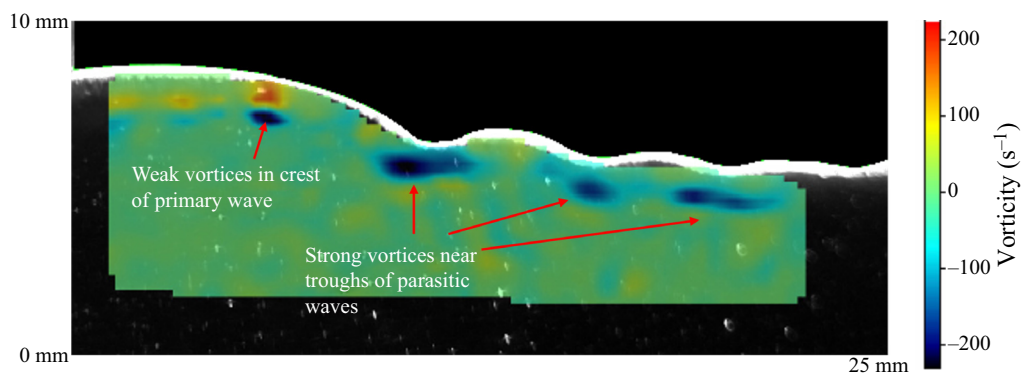


Figure 15. Velocity field and vorticity beneath parasitic waves. The inset is an expanded region of the lower figure. The x and z axes only show the scale, not the exact coordinates. Negative vorticity represents clockwise rotation.

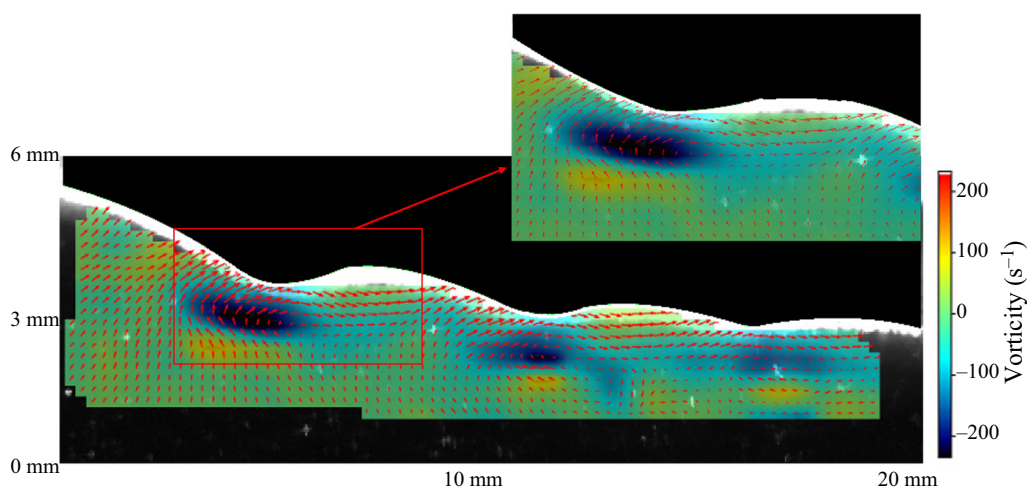


Figure 16. Vorticity beneath primary and parasitic waves. The x and z axes only show the scale, not the exact coordinates.

been demonstrated in the previous section. The lower edge of the illuminated boundary is established as the air–sea interface, and the velocity field beneath this interface is computed. Using PIV, the vorticity beneath parasitic waves on a 6 Hz primary wave is obtained, as shown in figure 15. As can be seen in the figure, high clockwise vorticity occurs on the crest side of the parasitic trough. This shows that the presence of wind is not necessary to form the parasitic waves and the vorticity beneath them. The high-vorticity areas beneath parasitic troughs generate anticlockwise vortices immediately beneath them, which shows that vorticity diffuses into the interior of the fluid. The vortices observed in this study are much stronger than the experimental results in Lin & Perlin (2001) and the numerical results in Mui & Dommermuth (1995) and Hung & Tsai (2009). This is because the parasitic waves shown in this study are much steeper than those in the previous studies. Highly vortical regions beneath the primary crest (capillary roller or bore) predicted by Longuet-Higgins (1992) are not observed. However, the weak vortex in the crest of the gravity–capillary wave predicted in Mui & Dommermuth (1995) is observed in this study (see figure 16). The evolution of vorticity for a 6 Hz primary wave is shown in figure 17

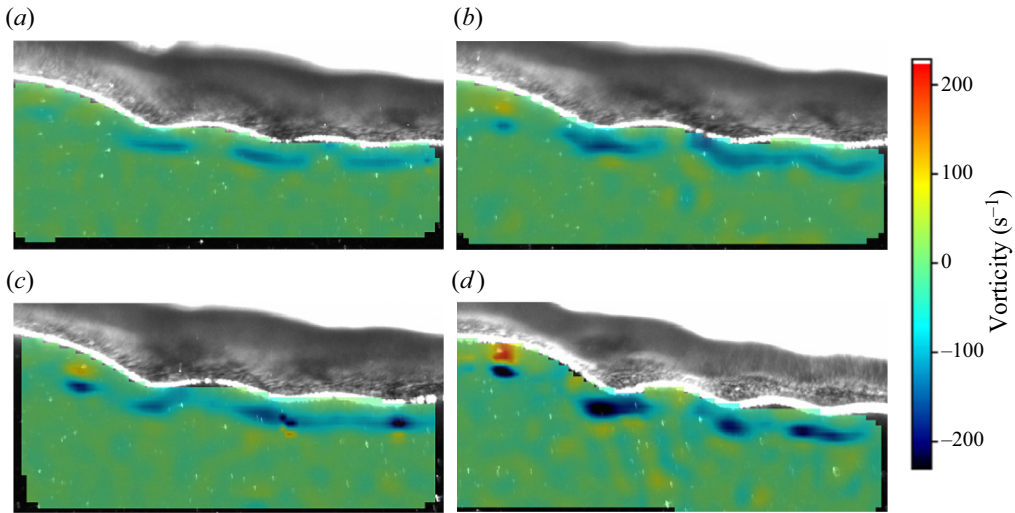


Figure 17. Evolution of vorticity beneath primary and parasitic waves: (a) $t = 0$ s; (b) $t = 0.02$ s; (c) $t = 0.04$ s; (d) $t = 0.06$ s.

as the wave propagates. Figure 17(d) is the same time as figure 16. It can be seen that the vorticity beneath the parasitic waves becomes more intense as the wave propagates into the convergent area, as does the vortex on the crest. The high-vorticity regions propagate downstream with the parasitic waves.

3.3. Energy dissipation due to parasitic waves

Parasitic waves are of small scale, which makes them more susceptible to viscous dissipation. The energy dissipated by parasitic waves comes from the primary waves as they are the drivers of the motion. According to the numerical simulations by Deike *et al.* (2015), the parasitic wave dissipation rate in gravity–capillary waves is comparable to the spilling and plunger breakers in gravity waves. In Zhang (2002), the dissipation rate enhanced by parasitic waves was calculated by summing the linear dissipation rate of all parasitic waves. This may underestimate the dissipation rate in the experiments here as the parasitic waves are highly nonlinear. Rather, the dissipation rate caused by the parasitic waves is evaluated by the dissipation function, which can be directly calculated using the velocity field. The dissipation rate caused by viscosity on a unit volume of fluid in a two-dimensional flow can be written as

$$\phi = \mu \left[2 \left(\frac{\partial u}{\partial x} \right)^2 + 2 \left(\frac{\partial w}{\partial z} \right)^2 + \left(\frac{\partial u}{\partial x} + \frac{\partial u}{\partial z} \right)^2 \right], \quad (3.1)$$

where μ is the dynamic viscosity of water and u and w are the x - and z -component velocities, respectively. The wave-height-based Reynolds number is

$$Re = \frac{uH}{\nu} = 1400. \quad (3.2)$$

The flow is considered laminar here, and it is reasonable to assume that the flow is axisymmetric, so that no turbulence dissipation term (from the velocity fluctuation) need be included. Neglecting the boundary layer effect and the heat transfer on the air–water

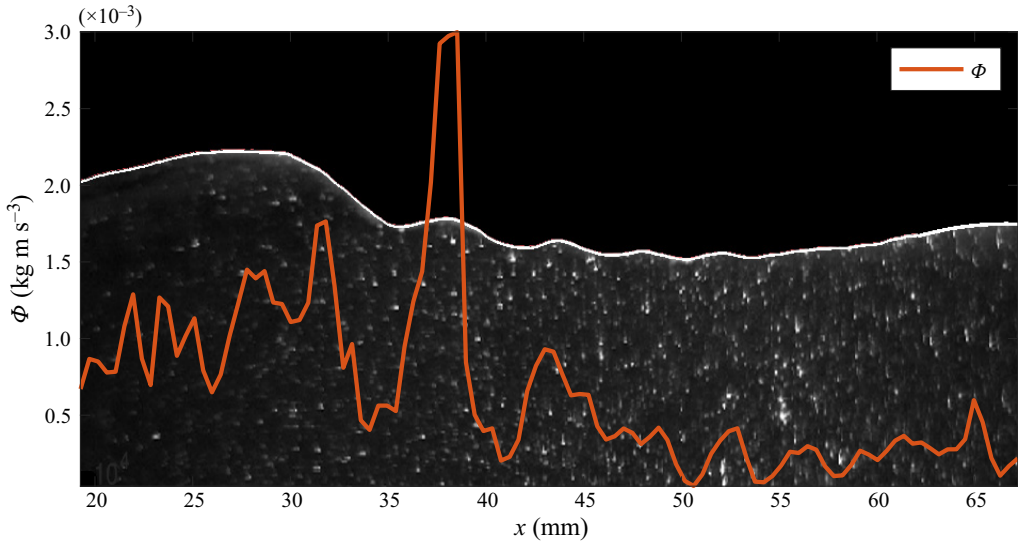


Figure 18. Dissipation function of a 6 Hz wave with parasitic capillary waves.

interface, the mechanical energy dissipation rate is fully represented by (3.1). This study focuses on the dissipation rate near the free surface; thus the calculation domain is from the free surface to $\lambda/2$ below the surface, where λ is the wavelength. The total dissipation rate at a given x position is obtained by multiplying the two-dimensional energy dissipation function ϕ by the corresponding arc length $r(x)$:

$$\Phi = \int_{-(\lambda/2)}^{\eta} \phi r(x) dz. \quad (3.3)$$

Thus Φ represents the depth-integrated energy dissipation rate across the arc per unit length. At one instant, for a 6 Hz primary wave, the energy dissipation rate along a wave crest and the parasitic waves is shown in figure 18. In the figure, the x axis is the distance along the centre laser sheet. It can be seen in the figure that the dissipation rate reaches its peak directly beneath the first parasitic crest. The wave crest dissipates more energy than the trough, and the first parasitic wave contributes most of the dissipation. Thus, it is evident that the presence of parasitic capillary waves significantly increases the dissipation rate, makes the primary waves more difficult to reach geometric, kinematic or dynamic breaking onset and hence prevents conventional breaking. The dissipation function distribution beneath a 6 Hz wave is shown in figure 19. In the figure, $\phi r(x)$ is shown for the same instant in figure 18. Rather than integrating over depth, figure 19(a) shows the dissipation rate distribution over space. To make a better comparison, the wave profile is shown in figure 19(b). It can be seen in the figure that the majority of dissipation occurs right beneath the first parasitic wave crest. The dissipation is not significant beneath a thin surface layer.

In addition to determine the energy dissipation, kinetic and potential energy components can be obtained using measured wave profiles and velocity fields. The kinetic energy over half a wavelength can be calculated by

$$KE = \frac{1}{2} \int_{-(\lambda/2)}^{\eta} \int_0^{\lambda/2} \rho(u^2 + v^2)r(x) dx dz, \quad (3.4)$$

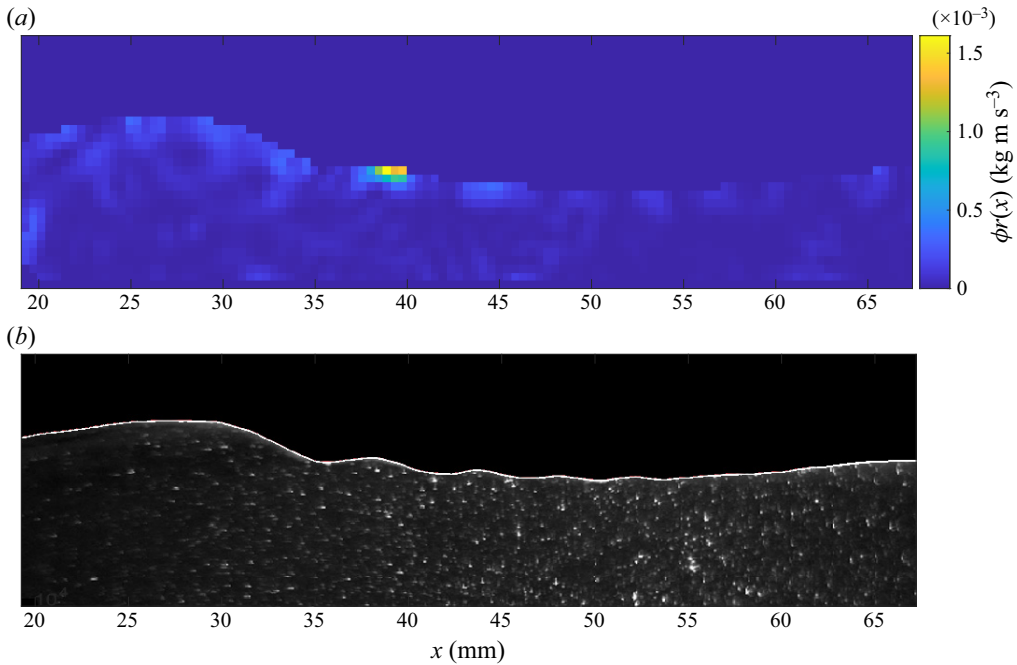


Figure 19. Dissipation function distribution in space of a 6 Hz wave with parasitic capillary waves. (a) Dissipation function distribution beneath a 6 Hz wave. (b) Profile of this 6 Hz wave.

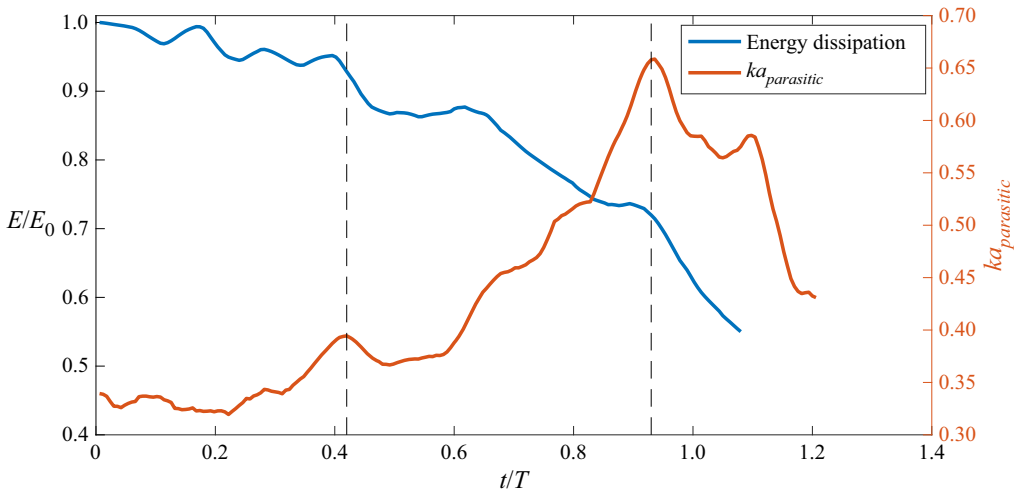


Figure 20. The variation of parasitic wave steepness and the dissipation of total energy in a 6 Hz primary wave case. Here E_0 is the initial total energy of the wave.

where $r(x)$ again is the arc length at a given x position. The potential energy over half a wavelength is given by

$$PE = \int_0^{\lambda/2} \rho g \frac{(\eta + h)^2 - h^2}{2} r(x) dx, \quad (3.5)$$

where η is the wave elevation and h is the mean water depth.

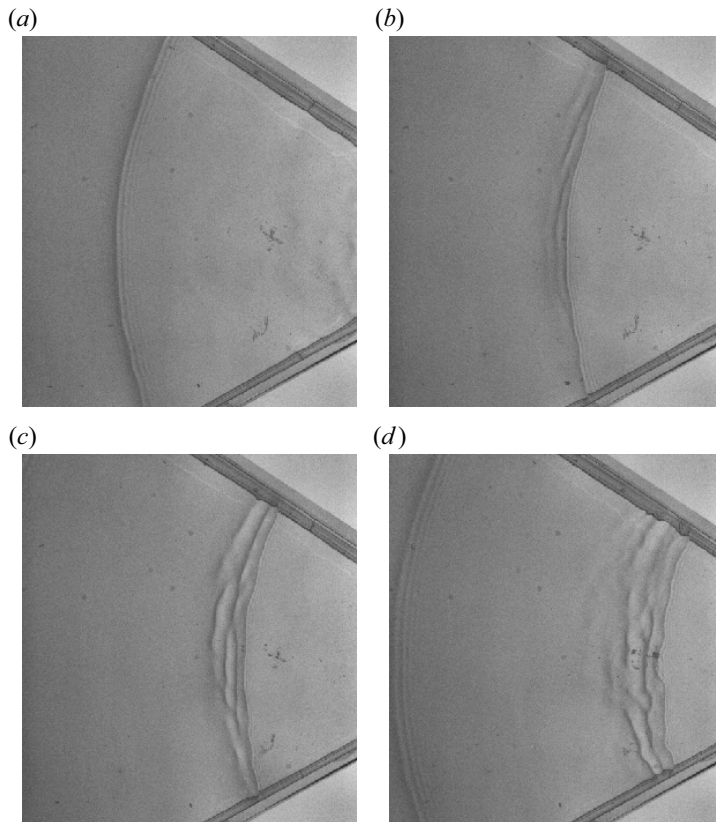


Figure 21. Overhead shadowgraph view of a time series of spatial images of a breaking 4.5 Hz wave with a surfactant-laden surface, case 6: (a) $t = 0$ s; (b) $t = 0.06$ s; (c) $t = 0.12$ s; (d) $t = 0.18$ s.

Obviously, the steepness of the parasitic wave does not increase indefinitely. In the experiments, it is found that the steepness varies as the wave propagates. Figure 20 presents the variation of the parasitic wave steepness and dissipation of the total energy ($PE + KE$) over half a wavelength; here, the steepness is calculated from the first parasitic wave near the crest, and the total energy is calculated using (3.4) and (3.5). It can be seen in the figure that a larger steepness of the parasitic wave leads to a higher dissipation rate, and that the peaks of the steepness are correlated highly with the large negative slope of the energy dissipation curve.

4. Micro-breaking of gravity–capillary waves

Herein micro-breaking is defined as breaking of gravity–capillary waves. Although parasitic waves dissipate a significant amount of energy of the primary waves, in some cases with reduced surface tension, the primary waves still achieve breaking onset and subsequent breaking. At the scale of gravity–capillary waves, the breaking is not always easily visible. Unlike plunging or spilling breakers in gravity waves, micro-breaking does not produce whitecapping or air entrainment, and therefore does not exhibit acoustic and other signatures. However, micro-breaking has similar dynamics to regular breaking, such as changing the wave profile from regular to irregular and dissipating significant amounts of energy during the breaking process. As the breaking process is subtle, detecting it

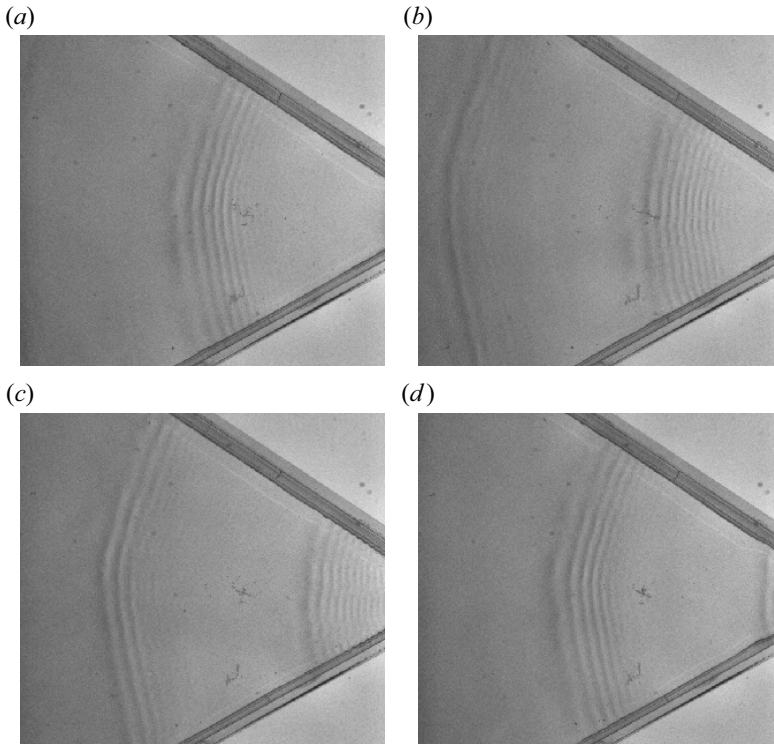


Figure 22. Parasitic waves on primary 4.5 Hz wave without surfactant: (a) $t = 0$ s; (b) $t = 0.07$ s; (c) $t = 0.14$ s; (d) $t = 0.21$ s.

becomes challenging. In this section, the shadowgraph technique is used to detect wave breaking on a two-dimensional surface, and both PLIF and PIV are utilized to measure and analyse the breaking process. In this study, breaking is assumed to occur when the wave profiles exhibit irregularity in the shadowgraph images. When using PIV, breaking is assumed when large vorticity is observed.

4.1. *Detection and visualization of micro-breaking*

Gravity–capillary waves are generated in the convergent channel, with surfactant added, using the circular wavemaker paddle. The range of the excitation frequency is 4 to 7 Hz. In the experiments, micro-breaking waves are observed in the middle or near the end of the convergent channel, depending on the excitation frequency. The signature of breaking exhibits a dramatic change of the wave profile during the process. It is more obvious in the shadowgraph images than in the two-dimensional PLIF and PIV images. This is because when the wave breaks, it rapidly becomes non-axisymmetric, and the information from a two-dimensional (x, z) measurement becomes limited.

Figure 21 shows the breaking process of a 4.5 Hz wave with added surfactant, captured by the shadowgraph technique. It can be seen in figure 21(a) that the wave starts with a clean axisymmetric crest, with some small parasitic waves on the forward crest face. As it propagates further, due to the convergence, the energy density increases and the wave starts to steepen and eventually breaks, as shown in figure 21(b). Unlike spilling or plunging breakers, the breaking process occurs on the rear side of the crest. As the wave propagates further, the breaking process becomes more obvious (figure 21c), and the rear edge of the

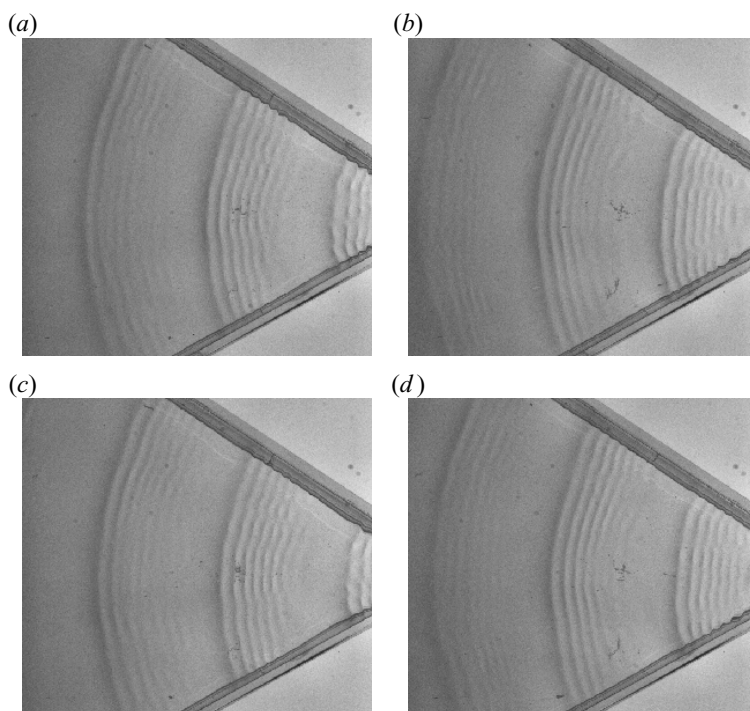


Figure 23. Parasitic waves on a 6 Hz wave without surfactant present: (a) $t = 0$ s; (b) $t = 0.1$ s; (c) $t = 0.2$ s; (d) $t = 0.3$ s. Clearly the waves steepen as they propagate and develop a crest-wise instability and phase jumps.

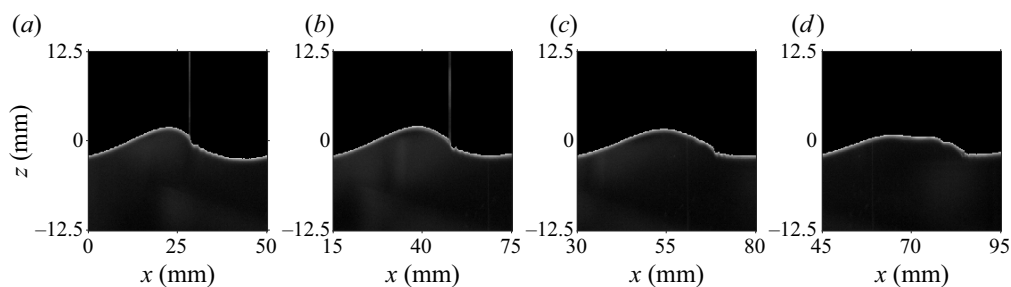


Figure 24. Wave profile of a breaking 5.5 Hz wave in the presence of surfactant. The vertical dimension of the images is exaggerated by a factor of two.

crest becomes more and more irregular. The process generates multiple short crests and becomes three-dimensional (no longer axisymmetric) as can be seen in [figure 21\(d\)](#).

For comparison, 4.5 Hz waves without surfactant are shown in [figure 22](#); the surfactant significantly suppressed the formation of the parasitic waves. As already mentioned, the surfactant reduces the surface tension, and hence reduces the pressure force that acts as a moving source on the surface. With fewer parasitic waves in the case with surfactant present, less energy is dissipated and the primary wave steepens. The energy dissipates eventually by micro-breaking. On the other hand, on the water surface without added surfactant, the parasitic waves dissipate most of the energy, and thus prevent the wave from breaking.

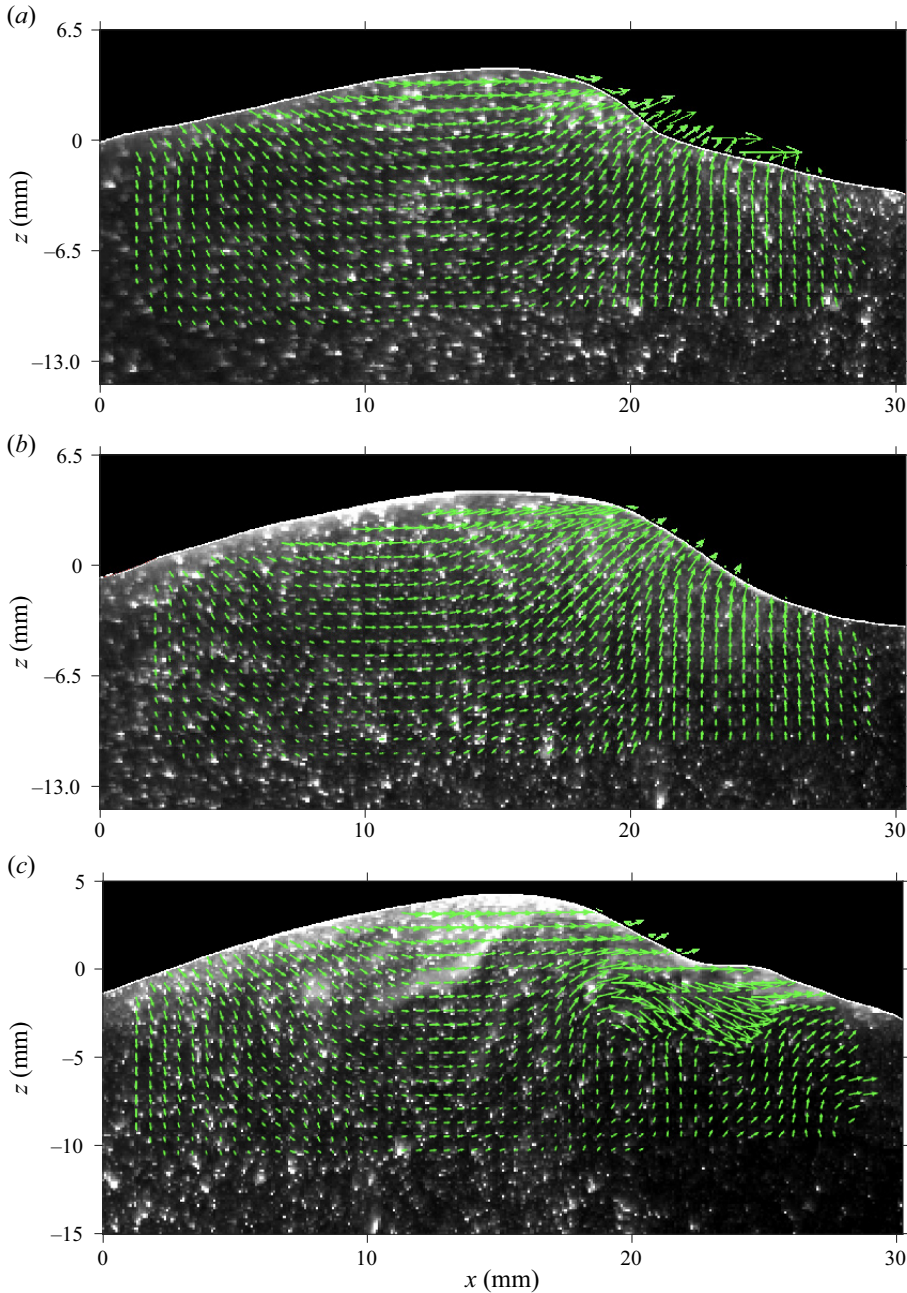


Figure 25. Velocity field beneath a breaking 6 Hz wave with surfactant present: (a) $t = 0$ s, before breaking; (b) $t = 0.05$ s, incipient breaking; (c) $t = 0.1$ s, breaking in progress.

As the waves propagate into a smaller arc in the convergent tank, the parasitic waves become steeper. This gives rise to nonlinear instabilities of the parasitic waves, and they depart from axisymmetry, and become three-dimensional. Using shadowgraphs, the three-dimensional instabilities are observed. [Figure 23](#) shows the evolution of the primary and parasitic waves under 6 Hz excitation with no surfactant present. It can be seen from

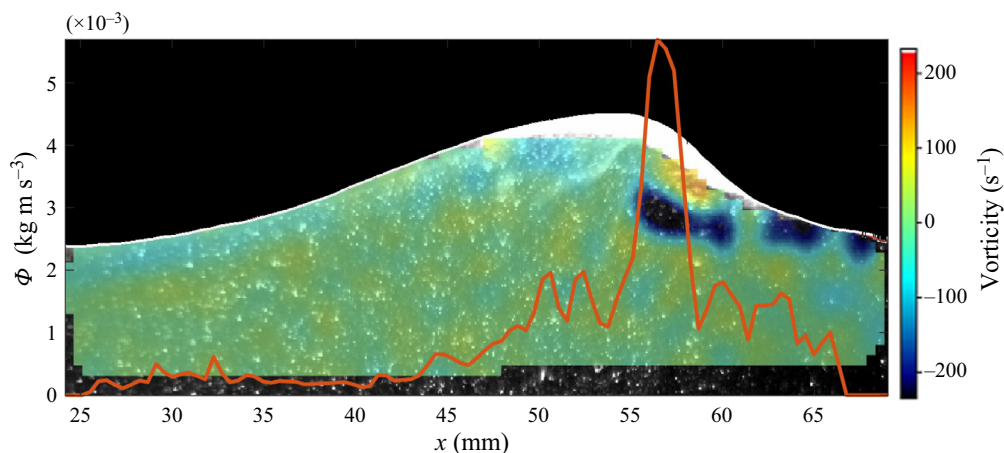


Figure 26. Dissipation rate (red curve) and vorticity field of a breaking 6 Hz wave.

the figure that, as the wave propagates to a narrower region, the parasitic waves become obviously steeper. There are approximately seven parasitic wave crests observed on the forward side of each primary wave crest. Although no breaking is observed, the parasitic waves still become non-axisymmetric near the end of the tank, and phase shifts can be seen along a parasitic wave crest. This is caused by nonlinear instabilities of the steep parasitic waves. More details of this instability could be investigated, but it is beyond the scope of this investigation.

The PLIF images of the breaking-process evolution of one crest of a 5.5 Hz wave are shown in figure 24. Surfactant is present so that the wave exhibits micro-breaking. Figure 24(a) shows a wave crest with some parasitic waves on the forward side. As it propagates, the crest leans forward, and the wave amplitude decreases. At the first bulge, the local slope becomes steeper, and eventually the primary wave crest merges into the parasitic waves (figure 24c). At this point, the wave elevation decreases significantly and a flattened area can be seen on the crest. Beyond this, a high-vorticity region is generated under the primary wave crest. This is consistent with the shadowgraph image, where multiple irregular crests occur on the rear side of the main crest.

4.2. Velocity field and micro-breaking onset

During the breaking process, a high-vorticity region is expected to occur in the vicinity of the primary wave crest. And, one assumes that the vorticity will be strengthened and expanded as breaking continues. This is investigated in the experiments using PIV. A velocity field during the breaking process of a 6 Hz wave is shown in figure 25, which presents one crest as it propagates. From top to bottom, the waves evolve from before breaking, to incipient breaking, to active breaking. It can be seen in the figure that before breaking, the wave profile becomes asymmetric and leans forward ($t = 0$ s). When the wave reaches breaking onset, vorticity starts to form under the first parasitic wave ($t = 0.05$ s). During the breaking process, increased vorticity is generated and the surface becomes irregular ($t = 0.1$ s). The associated vorticity during the breaking process is quantitatively shown in figure 26, the largest vorticity strength occurring on the forward side of the crest, where the energy dissipation rate also reaches a maximum. The vorticity is positive (anticlockwise rotation) close to the interface. A strong

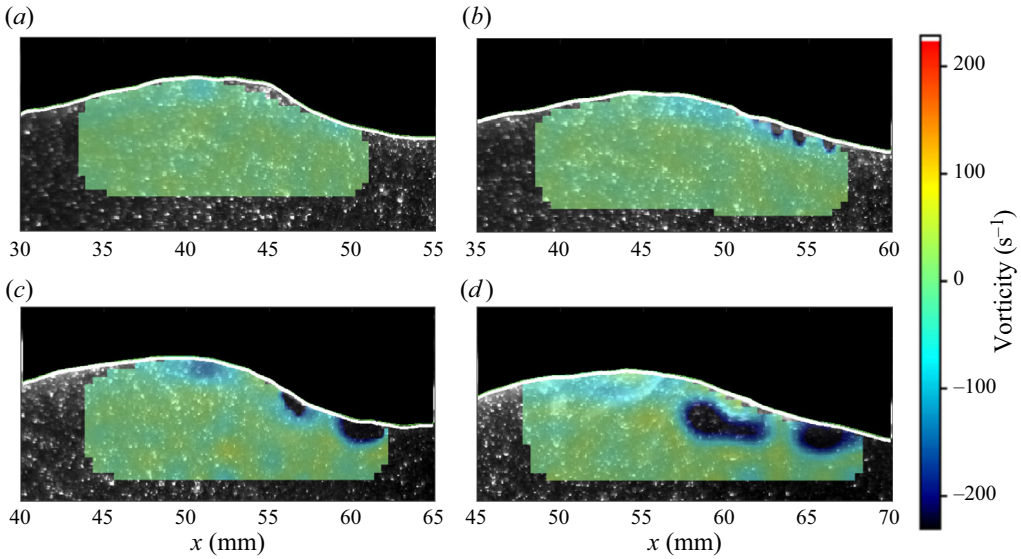


Figure 27. Evolution of vorticity in the micro-breaking process: (a) $t = 0.02$ s; (b) $t = 0.04$ s; (c) $t = 0.06$ s; (d) $t = 0.08$ s.

Reference	Wave type	Generation	Wave frequency (Hz)	u/c_p
Perlin, He & Bernal (1996)	Plunger	Dispersive focusing	1.4	0.74
Chang & Liu (1998)	Plunger	Shallow water	1	0.86
Qiao & Duncan (2001)	Spilling	Dispersive focusing	1.15–1.42	0.75–0.95
Oh <i>et al.</i> (2005)	Spilling	Wind	1.6–3	0.75
Na <i>et al.</i> (2020)	Spilling	Dispersive focusing	0.9	1.1

Table 3. Experimental studies of kinematic breaking onset in the literature.

negative-vorticity (clockwise rotation) region occurs right beneath the positive-vorticity region. The evolution of vorticity is shown in figure 27. As can be seen in the figure, vorticity is not observed at $t = 0.02$ s, while a small area of vorticity can be observed at $t = 0.04$ s. The area and intensity of the vorticity continue to grow as the wave propagates. At $t = 0.08$ s (figure 27d), the breaking is occurring and large vorticity is observed. The particle speed in the crest keeps increasing as the wave propagates. The maximum particle speed is 0.14 m s^{-1} at $t = 0$ s, while the maximum particle speed increases to 0.24 m s^{-1} at $t = 0.05$ s. Meanwhile, the variation of the phase velocity is very small. At incipient breaking, the ratio increases to $u/c_p = 0.78$. The kinematic onset of wave breaking has been widely studied experimentally for gravity waves. However, examination of kinematic criteria is non-trivial, and the onset is highly dependent on the method of generating the breaking waves. Table 3 shows some kinematic breaking onsets reported in the literature, all for gravity waves.

Table 4 shows the parameters for micro-breaking onset recorded in this study. It can be seen from table 4 that, as the wave shortens, the onset steepness becomes smaller, but the ratio of particle to phase speed increases. Surface tension plays a significant role in micro-breaking. The breaking type often depends on the Bond number and the wave steepness. Although breaking onsets have been studied widely, parameters for breaking

Case number	Frequency (Hz)	Wavelength (cm)	ka	u (m s^{-1})	c_p (m s^{-1})	u/c_p	Bo
7	4.5	7.85	0.34	0.24	0.35	0.68	51.0
8	5.5	5.37	0.31	0.20	0.29	0.70	23.9
9	6.0	4.58	0.28	0.21	0.27	0.78	17.4

Table 4. Wave parameters at onset of breaking, with added surfactant.

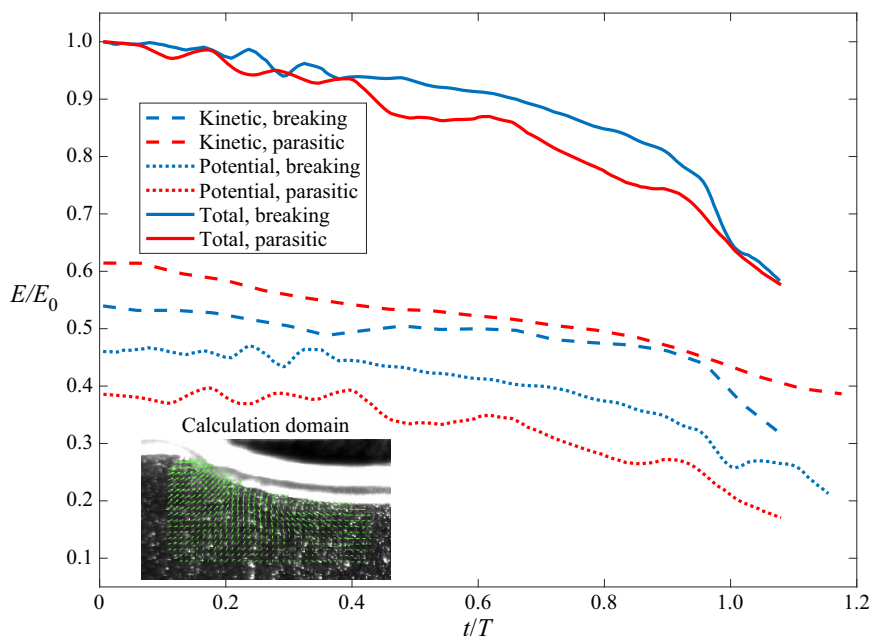


Figure 28. Energy evolution of parasitic waves and micro-breaking. Blue curves: waves with surfactant (breaking); red curves: waves without surfactant (parasitic); solid curves: total energy; dashed curves: kinetic energy; dotted curves: potential energy.

waves at small scales are virtually absent in the literature. For the same Bond number and steepness in two-dimensional facilities, only parasitic capillary waves have been presented in the literature, and no breaking waves have been reported. Thus, the convergent channel coupled with added surfactant facilitates wave breaking.

4.3. Energy dissipation during micro-breaking

The energy dissipation rate of a breaking 5.5 Hz wave is shown in figure 26. It is obtained using the same method as described in § 3.3. The maximum dissipation rate appears on the forward side of the crest where the primary wave crest merges into the parasitic wave. It can also be seen in figure 26 that the maximum dissipation rate occurs in the vicinity of the highest vorticity. By comparing the instantaneous dissipation rate of the parasitic waves and micro-breaking in figures 18 and 26, it can be concluded that the dissipation rate of micro-breaking is much higher than the dissipation rate of parasitic capillary waves. After breaking, the wave no longer retains its regular profile and the wave elevation decreases significantly. In the parasitic wave cases, although parasitic waves dissipate

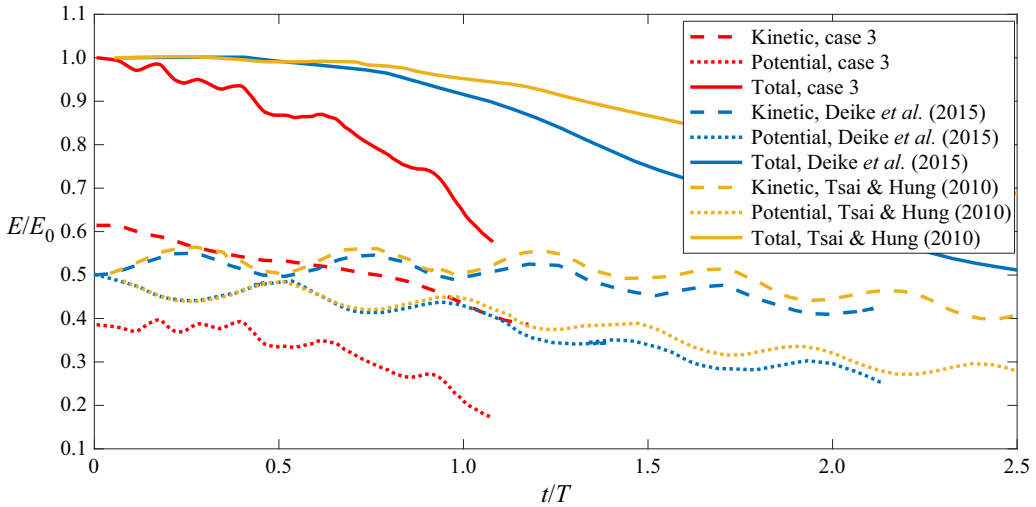


Figure 29. Energy evolution of waves with parasitic waves. Two numerical studies in the literature and the present experiments. In Tsai & Hung (2010, figure 1*f,g,h*), $\lambda = 5$ cm, $ka = 0.28$ is selected. In Deike *et al.* (2015, figure 8*e*), $Bo = 10$, $ka = 0.3$ is selected. Case 3 in this study: $Bo = 8.34$, $\lambda = 4.85$ cm, $ka = 0.26$.

energy, the primary waves are able to maintain their wave elevation. However, the total energy dissipated through parasitic waves is comparable to the energy dissipated through the breaking process. As figures 18 and 26 only show the instantaneous energy dissipation rate, the parasitic waves persist for the entire propagation, while breaking only occurs for a shorter period of time. For the breaking cases, due to added surfactant, the parasitic waves are generally suppressed.

In figure 28, the potential and kinetic energy evolution is shown for waves with parasitic waves and waves with added surfactant (micro-breaking waves). The data are from the 6 Hz wave experiments (case 3 in table 1 and case 9 in table 4). The energy is calculated using the wave profile (potential) and velocity field (kinetic); (3.4) and (3.5) are used for this calculation. Thus the total energy of half of the wavelength is considered (shown in the figure). The energy evolution of one particular wave segment is calculated by propagating the calculation domain with the wave, at the phase speed. Here E represents the instantaneous energy, E_0 is the initial total energy and T is the wave period. The initial energy calculation does not start from the first wave near the wavemaker, but from the starting point of the laser sheet. Initially, the dissipation rate of the two waves is close, but by $t/T = 0.4$, the parasitic waves are dissipating more. However, at approximately $t/T = 0.95$, the breaking process starts on the waves with added surfactant, and the dissipation rate increases significantly, as shown by the solid blue curve. The figure also shows that the ratio of potential energy and kinetic energy is not 1 : 1 as predicted by linear theory. In waves with surfactant, where parasitic waves are mostly absent, the initial kinetic energy contributes approximately 54 % of the total energy while the potential energy contribution is around 46 %. In the wave without surfactant but with parasitic waves, the contribution of kinetic energy increases to approximately 60 %, while the potential energy reduces to 40 %. This is different from the previous studies of waves before and during spilling or plunging breaking (Lim *et al.* 2015; Derakhti & Kirby 2016; Na *et al.* 2020). In the experiments herein, in a convergent channel, the parasitic waves experience an increase in the ratio of kinetic energy to total energy.

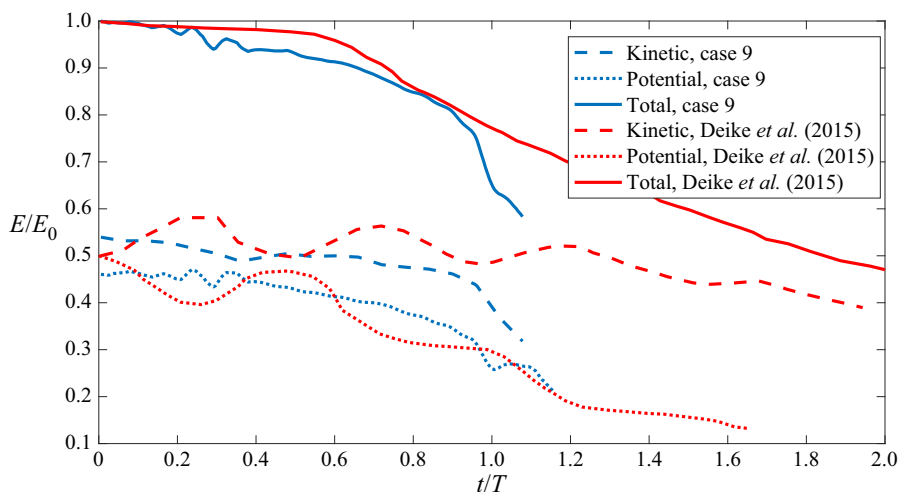


Figure 30. Energy evolution of small-scale breaking waves. In Deike *et al.* (2015, figure 8*f*), $ka = 0.45$, $Bo = 10$ is selected. Case 9 in this study, $Bo = 17.4$, $ka = 0.28$ is presented.

Figure 29 shows a comparison of the kinetic and potential energy evolutions of parasitic waves in this study with some selected numerical results in the literature. The numerical results for $\lambda = 5$ cm are selected, for comparison with case 3 ($\lambda = 4.85$ cm) in this study. It can be seen in the figure that the dissipation rate in this study is much higher than those in the numerical results. This is because the steeper parasitic waves in the convergent channel contribute stronger dissipation. Also, it is noted that in the numerical results, the ratio of potential and kinetic energy starts at 1. This is because in the numerical study at $t = 0$, the parasitic waves are yet to be generated, while in the experiments, there are already parasitic waves at the beginning of the measurement. Both numerical and experimental results show higher kinetic energy than potential energy after the generation of parasitic waves. It might be more suitable to start the numerical results at around $t/T = 1$ when comparing with the experimental results. It is also worth noting that the oscillation modes in the kinetic and potential energy in the numerical results are not observed in the experiments.

Comparison of energy evolution of small-scale breaking is shown in figure 30. Case 9 in the present study is compared with numerical results in Deike *et al.* (2015). In case 9, the primary wave steepness $ka = 0.28$. The Bond number $Bo = 17.4$, while in the case from Deike *et al.* (2015), $ka = 0.45$, $Bo = 10$. The two cases have similar Bond number, but the case in Deike *et al.* (2015) has much higher steepness and was categorized as a spilling breaker. It can be seen in the figure that the dissipation rate of the experimental results is close to the numerical one. The kinematic energy remains higher than the potential energy in both cases.

Two non-dimensional parameters are critical to the breaking pattern of waves: steepness ka and the Bond number Bo . Deike *et al.* (2015) showed a wave regime diagram with boundaries between different types of breaking waves, based on the numerical results. The figure is replotted here as figure 31. Three micro-breaking cases observed in this study are added to the diagram, shown as filled blue circles. It is noted that these micro-breaking cases are beneath the breaking boundary, in the parasitic capillary wave regime. To the best of the authors' knowledge, no breaking waves have been reported in this regime without wind, either numerical or experimental. This is as a consequence that almost

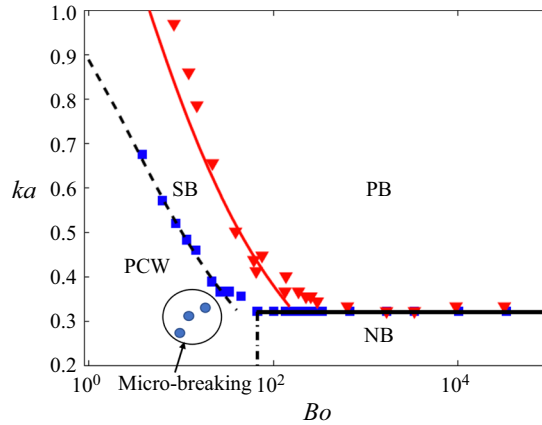


Figure 31. Wave regime diagram. The boundaries between the wave regimes obtained numerically in Deike *et al.* (2015, figure 7). PB: plunging breakers; SB: spilling breakers; PCW: parasitic capillary waves; NB: non-breaking gravity waves. Blue circles represent micro-breaking cases 7, 8, 9 in this study.

all previous numerical and experimental studies in this regime were conducted either in two-dimensions or in rectangular tanks, and the subsequent dissipation of parasitic waves prevented the breaking. Micro-breaking occurs in this study due to the increase of energy flux caused by spatial convergence.

5. Discussion and concluding remarks

Parasitic waves on gravity–capillary waves are studied experimentally; unlike previous studies where the waves propagate in a two-dimensional channel, this paper examined the parasitic waves in a convergent axisymmetric channel. This enables the parasitic waves to be generated in the absence of wind, and grow to the maximum steepness before they decay due to viscosity. To the authors’ knowledge, little work has been done on the experimental study of mechanically generated waves exhibiting parasitic capillaries since that of Perlin *et al.* (1993) and Jiang *et al.* (1999). Both geometric and dynamic features of the parasitic waves are studied. The wavelength of parasitic waves increases with the frequency of the primary waves. This is consistent with theoretical prediction. The parasitic waves become steeper when they propagate along the convergent channel, until they reach a maximum steepness. Shorter primary waves generate steeper parasitic waves. The energy dissipation rate increases as the steepness of the parasitic waves grows. For shorter primary waves, the parasitic waves become longer and interact with the primary waves. For primary waves above 8 Hz, parasitic waves and primary waves can hardly be differentiated. A high-vorticity region is observed beneath the trough of each parasitic wave; the high-vorticity region propagates with the parasitic wave. The instantaneous dissipation rate of waves is obtained using the viscous dissipation function. The results demonstrate that the highest dissipation rate occurs under the first parasitic bulge, where the parasitic wave is the steepest. Although the convergent channel increases the spatial energy density, the gravity–capillary waves do not break due to the enhanced energy dissipation of parasitic waves. When the parasitic waves are present, the kinetic energy in one wavelength is greater than the potential energy. When the parasitic waves are suppressed by surfactant, the ratio of kinetic energy to potential energy is close to 1 : 1.

Experiments show that adding surfactant significantly reduces the formation of parasitic waves, and as a result, the energy is not dissipated sufficiently to prevent the waves from breaking. Compared with plunging and spilling breakers of gravity waves, the breaking of gravity–capillary waves does not exhibit air entrainment, and is subtle. The micro-scale breaking waves are captured using the shadowgraph technique, and geometric, kinetic and kinematic features are measured using PLIF and PIV. Unlike waves on surfaces without added surfactant, these waves are almost free of parasitic waves; thus, the waves steepen and eventually break in the convergent channel. The geometric and kinematic breaking threshold for micro-breaking in a convergent channel is lower than the spilling and plunging breaking threshold for two-dimensional gravity waves. Micro-breaking gravity–capillary waves without wind are basically unexploited in the literature, both numerical and experimental, and need to be considered when studying general wave-breaking criteria.

Declaration of interests. The authors report no conflict of interest.

Author ORCIDs.

Chang Xu <https://orcid.org/0000-0002-8764-3548>;

Marc Perlin <https://orcid.org/0000-0003-3590-2867>.

REFERENCES

- BABANIN, A. 2011 *Breaking and Dissipation of Ocean Surface Waves*. Cambridge University Press.
- BARTHELEMY, X., BANNER, M.L., PEIRSON, W.L., FEDELE, F., ALLIS, M. & DIAS, F. 2018 On a unified breaking onset threshold for gravity waves in deep and intermediate depth water. *J. Fluid Mech.* **841**, 463–488.
- CAULLIEZ, G. 2013 Dissipation regimes for short wind waves. *J. Geophys. Res.: Oceans* **118** (2), 672–684.
- CHABANE, M. & CHOI, W. 2019 On resonant interactions of gravity–capillary waves without energy exchange. *Stud. Appl. Maths* **142** (4), 528–550.
- CHANG, K.-A. & LIU, P.L.-F. 1998 Velocity, acceleration and vorticity under a breaking wave. *Phys. Fluids* **10** (1), 327–329.
- COX, C.S. 1958 Measurements of slopes of high-frequency wind waves. *J. Mar. Res.* **16**, 199–225.
- CRAPPER, G.D. 1970 Non-linear capillary waves generated by steep gravity waves. *J. Fluid Mech.* **40** (1), 149–159.
- DEAN, R.G. & DALRYMPLE, R.A. 1991 *Water Wave Mechanics for Engineers and Scientists*, vol. 2. World Scientific Publishing Company.
- DEIKE, L., POPINET, S. & MELVILLE, W.K. 2015 Capillary effects on wave breaking. *J. Fluid Mech.* **769**, 541–569.
- DERAKHTI, M., BANNER, M.L. & KIRBY, J.T. 2018 Predicting the breaking strength of gravity water waves in deep and intermediate depth. *J. Fluid Mech.* **848**, R2.
- DERAKHTI, M. & KIRBY, J.T. 2014 Bubble entrainment and liquid–bubble interaction under unsteady breaking waves. *J. Fluid Mech.* **761**, 464–506.
- DERAKHTI, M. & KIRBY, J.T. 2016 Breaking-onset, energy and momentum flux in unsteady focused wave packets. *J. Fluid Mech.* **790**, 553–581.
- DOSAIEV, A., TROITSKAYA, Y.I. & SHRIRA, V.I. 2021 On the physical mechanism of front–back asymmetry of non-breaking gravity–capillary waves. *J. Fluid Mech.* **906**, A11.
- DUNCAN, J.H. 2001 Spilling breakers. *Annu. Rev. Fluid Mech.* **33** (1), 519–547.
- DUNCAN, J.H., QIAO, H., PHILOMIN, V. & WENZ, A. 1999 Gentle spilling breakers: crest profile evolution. *J. Fluid Mech.* **379**, 191–222.
- FEDOROV, A.V. & MELVILLE, W.K. 1998 Nonlinear gravity–capillary waves with forcing and dissipation. *J. Fluid Mech.* **354**, 1–42.
- FEDOROV, A.V., MELVILLE, W.K. & ROZENBERG, A. 1998 An experimental and numerical study of parasitic capillary waves. *Phys. Fluids* **10** (6), 1315–1323.
- HUANG, N.E., SHEN, Z., LONG, S.R., WU, M.C., SHIH, H.H., ZHENG, Q., YEN, N.-C., TUNG, C.C. & LIU, H.H. 1998 The empirical mode decomposition and the Hilbert spectrum for nonlinear and non-stationary time series analysis. *Proc. R. Soc. Lond. A* **454** (1971), 903–995.

- HUNG, L.-P. & TSAI, W.-T. 2009 The formation of parasitic capillary ripples on gravity–capillary waves and the underlying vortical structures. *J. Phys. Oceanogr.* **39** (2), 263–289.
- IARFATI, A. 2009 Numerical study of the effects of the breaking intensity on wave breaking flows. *J. Fluid Mech.* **622**, 371–411.
- JESSUP, A.T., ZAPPA, C.J., LOEWEN, M.R. & HESANY, V. 1997 Infrared remote sensing of breaking waves. *Nature* **385** (6611), 52.
- JIANG, L., LIN, H.-J., SCHULTZ, W.W. & PERLIN, M. 1999 Unsteady ripple generation on steep gravity–capillary waves. *J. Fluid Mech.* **386**, 281–304.
- KHAIT, A. & SHEMER, L. 2018 On the kinematic criterion for the inception of breaking in surface gravity waves: fully nonlinear numerical simulations and experimental verification. *Phys. Fluids* **30** (5), 057103.
- KIGER, K.T. & DUNCAN, J.H. 2012 Air-entrainment mechanisms in plunging jets and breaking waves. *Annu. Rev. Fluid Mech.* **44**, 563–596.
- LAXAGUE, N.J.M., ZAPPA, C.J., LEBEL, D.A. & BANNER, M.L. 2018 Spectral characteristics of gravity–capillary waves, with connections to wave growth and microbreaking. *J. Geophys. Res.: Oceans* **123** (7), 4576–4592.
- LIM, H.-J., CHANG, K.-A., HUANG, Z.-C. & NA, B. 2015 Experimental study on plunging breaking waves in deep water. *J. Geophys. Res.: Oceans* **120** (3), 2007–2049.
- LIN, H.J. & PERLIN, M. 2001 The velocity and vorticity fields beneath gravity–capillary waves exhibiting parasitic ripples. *Wave Motion* **33** (3), 245–257.
- LIU, X. & DUNCAN, J.H. 2003 The effects of surfactants on spilling breaking waves. *Nature* **421** (6922), 520.
- LONGUET-HIGGINS, M.S. 1963 The generation of capillary waves by steep gravity waves. *J. Fluid Mech.* **16** (1), 138–159.
- LONGUET-HIGGINS, M.S. 1992 Capillary rollers and bores. *J. Fluid Mech.* **240**, 659–679.
- LONGUET-HIGGINS, M.S. 1995 Parasitic capillary waves: a direct calculation. *J. Fluid Mech.* **301**, 79–107.
- MELVILLE, W.K. 1982 The instability and breaking of deep-water waves. *J. Fluid Mech.* **115**, 165–185.
- MELVILLE, W.K. & FEDOROV, A.V. 2015 The equilibrium dynamics and statistics of gravity–capillary waves. *J. Fluid Mech.* **767**, 449–466.
- MILLER, R.L. 1973 *The Role of Surface Tension in Breaking Waves*, pp. 433–449. American Society of Civil Engineers.
- MUI, R.C.Y. & DOMMERMUTH, D.G. 1995 The vortical structure of parasitic capillary waves. *Trans. ASME J. Fluids Engng* **117**, 355–361.
- NA, B., CHANG, K. & LIM, H. 2020 Flow kinematics and air entrainment under laboratory spilling breaking waves. *J. Fluid Mech.* **882**, A15.
- NEPF, H.M., WU, C.H. & CHAN, E.S. 1998 A comparison of two- and three-dimensional wave breaking. *J. Phys. Oceanogr.* **28** (7), 1496–1510.
- OH, S.-H., MIZUTANI, N., SUH, K.-D. & HASHIMOTO, N. 2005 Experimental investigation of breaking criteria of deepwater wind waves under strong wind action. *Appl. Ocean Res.* **27** (4–5), 235–250.
- PERLIN, M., HE, J. & BERNAL, L.P. 1996 An experimental study of deep water plunging breakers. *Phys. Fluids* **8** (9), 2365–2374.
- PERLIN, M., LIN, H. & TING, C.-L. 1993 On parasitic capillary waves generated by steep gravity waves: an experimental investigation with spatial and temporal measurements. *J. Fluid Mech.* **255**, 597–620.
- QIAO, H. & DUNCAN, J.H. 2001 Gentle spilling breakers: crest flow-field evolution. *J. Fluid Mech.* **439**, 57–85.
- RAMBERG, S.E., BARBER, M.E. & GRIFFIN, O.M. 1985 Laboratory studies of steep and breaking deep water waves in a convergent channel. *Report*. Naval Research Lab, Washington DC.
- RAMBERG, S.E. & GRIFFIN, O.M. 1987 Laboratory study of steep and breaking deep water waves. *ASCE J. Waterway Port Coastal Ocean Engng* **113** (5), 493–506.
- RAPP, R.J. & MELVILLE, W.K. 1990 Laboratory measurements of deep-water breaking waves. *Phil. Trans. R. Soc. Lond. A* **331** (1622), 735–800.
- SAKET, A., PEIRSON, W.L., BANNER, M.L., BARTHELEMY, X. & ALLIS, M.J. 2017 On the threshold for wave breaking of two-dimensional deep water wave groups in the absence and presence of wind. *J. Fluid Mech.* **811**, 642–658.
- SHE, K., GREATED, C.A. & EASSON, W.J. 1994 Experimental study of three-dimensional wave breaking. *ASCE J. Waterway Port Coastal Ocean Engng* **120** (1), 20–36.
- SIDDIQUI, M.H.K., LOEWEN, M.R., RICHARDSON, C., ASHER, W.E. & JESSUP, A.T. 2001 Simultaneous particle image velocimetry and infrared imagery of microscale breaking waves. *Phys. Fluids* **13** (7), 1891–1903.
- TSAI, W.-T. & HUNG, L.-P. 2010 Enhanced energy dissipation by parasitic capillaries on short gravity–capillary waves. *J. Phys. Oceanogr.* **40** (11), 2435–2450.

- WU, C.H. & NEPF, H.M. 2002 Breaking criteria and energy losses for three-dimensional wave breaking. *J. Geophys. Res.: Oceans* **107** (C10), 3177.
- XU, C. & PERLIN, M. 2021 Gravity–capillary multi-component wave patterns generated by a single-frequency wave-maker oscillation and subsequent resonances. *J. Fluid Mech.* **926**, A39.
- ZAPPA, C.J., ASHER, W.E. & JESSUP, A.T. 2001 Microscale wave breaking and air–water gas transfer. *J. Geophys. Res.: Oceans* **106** (C5), 9385–9391.
- ZHANG, X. 1995 Capillary–gravity and capillary waves generated in a wind wave tank: observations and theories. *J. Fluid Mech.* **289**, 51–82.
- ZHANG, X. 2002 Enhanced dissipation of short gravity and gravity capillary waves due to parasitic capillaries. *Phys. Fluids* **14** (11), L81–L84.